## nature physics

**Article** 

https://doi.org/10.1038/s41567-024-02600-2

## Optogenetic generation of leader cells reveals a force-velocity relation for collective cell migration

Received: 11 November 2022

Accepted: 3 July 2024

Published online: 12 August 2024



Check for updates

Leone Rossetti ©¹⊠, Steffen Grosser ©¹, Juan Francisco Abenza¹², Léo Valon **3**, Pere Roca-Cusachs **1**,4, Ricard Alert **5**,6,7 **2** & Xavier Trepat **©** 1,3,4,8 ⊠

During development, wound healing and cancer invasion, migrating cell clusters feature highly protrusive leader cells at their front. Leader cells are thought to pull and direct their cohort of followers, but whether their local action is enough to guide the entire cluster, or if a global mechanical organization is needed, remains controversial. Here we show that the effectiveness of the leader-follower organization is proportional to the asymmetry of traction and tension within cell clusters. By combining hydrogel micropatterning and optogenetic activation, we generate highly protrusive leaders at the edge of minimal cell clusters. We find that the induced leader can robustly drag one follower but not larger groups. By measuring traction forces and tension propagation in clusters of increasing size, we establish a quantitative relationship between group velocity and the asymmetry of the traction and tension profiles. Modelling motile clusters as active polar fluids, we explain this force-velocity relationship in terms of asymmetries in the active traction profile. Our results challenge the notion of autonomous leader cells, showing that collective cell migration requires global mechanical organization within the cluster.

Collective motion is a recurrent property of groups of self-propelled agents, including macromolecular assemblies, human crowds or robots swarms<sup>1-3</sup>. Although the coordination and function of these groups can emerge from interactions between identical constituents<sup>4,5</sup>, it is often mediated by specialized agents<sup>6</sup>. Small numbers of such agents can either disrupt or enhance group dynamics7-9, like in the case of animal groups guided by specialized individuals that act as leaders 10,11. Similarly, collectively migrating cells during development, wound healing or cancer invasion are thought to be guided by leader cells<sup>12-20</sup>.

Leader cells are found at the front edge of migrating groups, have a protrusive and polarized phenotype and are identified by the activity of specific signalling pathways 14,17,21-26. Conversely, the remaining cells are termed follower cells and are thought to be mechanically pulled and guided by their leaders through direct physical connections<sup>15,22,27-29</sup>. This description appears to capture many in vitro and in vivo phenomena. Epithelial cell sheets migrate by projecting multicellular outgrowths, with protrusive cells at their front 13,23,25 During branching morphogenesis, long cell strands are tipped by

<sup>1</sup>Institute for Bioengineering of Catalonia (IBEC), The Barcelona Institute for Science and Technology (BIST), Barcelona, Spain. <sup>2</sup>Centro de Investigación Biomédica en Red en Bioingeniería, Biomateriales y Nanomedicina (CIBER-BBN), Barcelona, Spain. 3 Department of Developmental and Stem Cell Biology, Institut Pasteur, CNRS UMR 3738, Paris, France. 4Facultat de Medicina, Universitat de Barcelona, Barcelona, Spain. 5Max Planck Institute for the Physics of Complex Systems, Dresden, Germany. 6Centre for Systems Biology Dresden, Dresden, Germany. 7Cluster of Excellence Physics of Life, TU Dresden, Dresden, Germany. <sup>8</sup>Institució Catalana de Recerca i Estudis Avançats (ICREA), Barcelona, Spain. 🖂 e-mail: lrossetti@ibecbarcelona.eu; ralert@pks.mpg.de; xtrepat@ibecbarcelona.eu

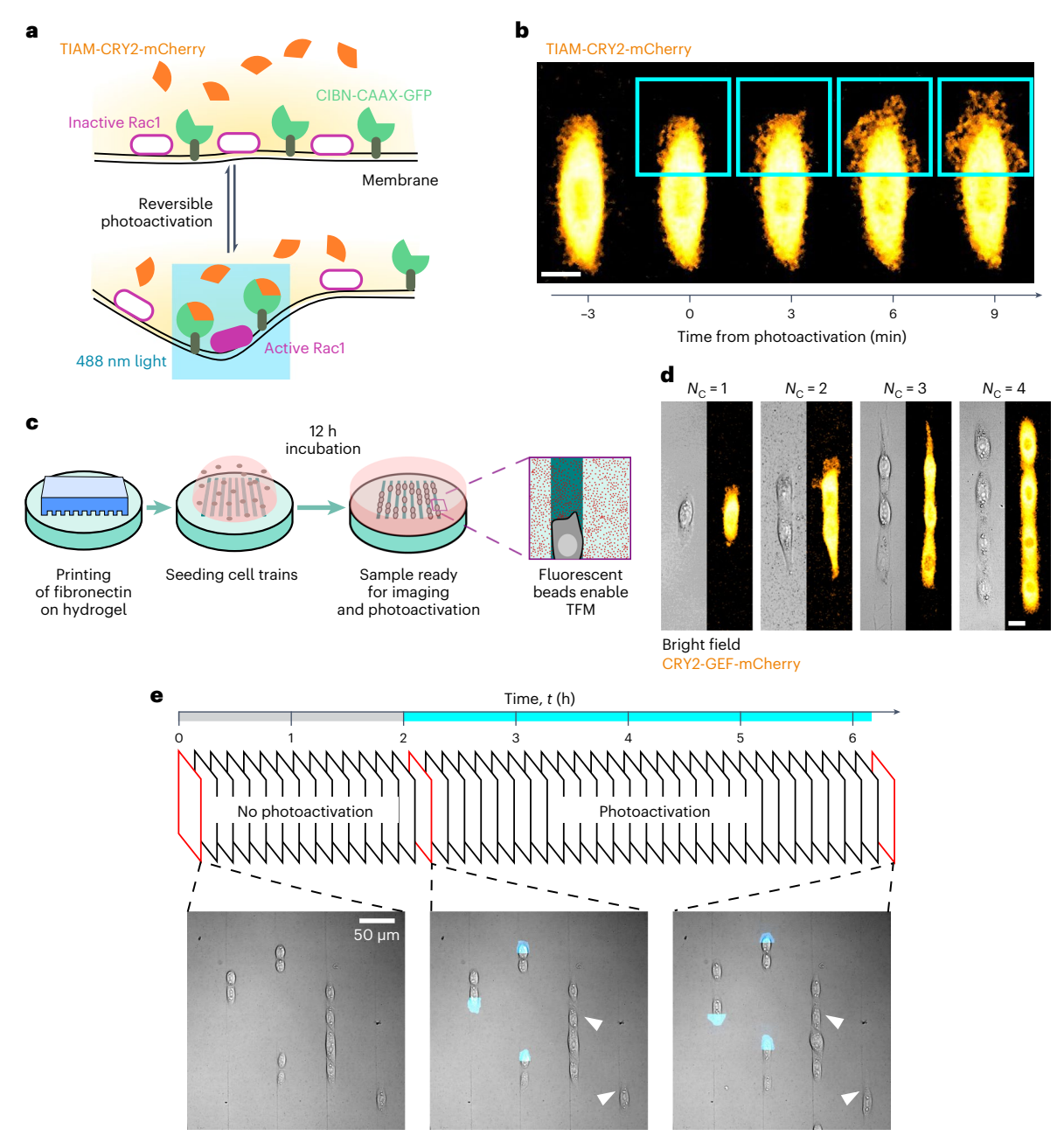


Fig. 1 | Optogenetic control of lamellipodium formation in cell trains. a, Scheme of the optogenetic system to control lamellipodium formation. OptoMDCK-Rac1 express two constructs: an activator of Rac1 fused to CRY2 and membrane-bound CIBN. On blue light illumination, CRY2 binds to CIBN, locally activating Rac1 and causing lamellipodium growth. b, Effect of photoactivation on a cell. 488 nm light is applied to the blue region every 3 min, inducing lamellipodium formation. Scale bar, 20  $\mu$ m. c, Scheme of sample preparation: microcontact printing of polyacrylamide hydrogels (E=18 kPa) with fibronectin

lines (width,  $20~\mu m$ ) and incubation with optoMDCK-Rac1 yields samples containing hundreds of cell trains of different lengths. The substrates are prepared with fluorescent beads, making them apt for TFM. **d**, Representative microscopy images of cell trains. Scale bar,  $20~\mu m$ . **e**, Scheme of the experimental protocol. Fields of view containing cell trains ( $N_c = [1, 4]$ ) are imaged for 2~h every 3 min without photoactivation; then, a subset of cell trains is photoactivated (blue regions) at every imaging interval, whereas other cell trains (white arrowheads) are left non-activated.

lamellipodium-generating cells $^{30,31}$ . Border cells are small clusters of ~8 cells that migrate during *Drosophila* oogenesis and have a polarized and protrusive cell at their front $^{27,32}$ . In some invasive tumours, strands of cells project out from a cluster following a single cancer cell or a cancer-associated fibroblast $^{26,33-35}$ .

Despite this extensive phenomenology, the fundamental mechanical organization enabling leader–follower coordination is still unclear. Two main scenarios are possible. One is that the local mechanical action of a leader is sufficient to drive collective migration, regardless of the behaviour of its followers. The other is that a global organization

of forces within the group is needed. Addressing this long-standing problem requires direct measurements of the relationship between collective cell velocity and the underlying spatial distribution of forces, but such a force–velocity relationship has not been reported. To fill this gap, we used optogenetics to induce leader cells in minimal groups of controlled size. We show that the generation of a leader is insufficient to drive the migration of groups larger than two cells. To understand this behaviour, we performed a systematic study of the mechanical conditions that enable collective cell migration in clusters of increasing cell number. This analysis revealed that for every cluster size, collective

cell migration requires an asymmetric distribution of traction forces on a multicellular scale. A model of the cell cluster as an active polar fluid establishes the relationship between migration velocity and the asymmetries of the underlying traction force field.

#### Generating leader cells using optogenetics

A hallmark of leader cells is lamellipodium formation by the activation of the small Rho GTPase Rac1 at their leading edge<sup>12,15,36</sup>. We reasoned that we could use optogenetics to locally activate Rac1 in cell groups, thereby creating leader cells on demand<sup>32,37,38</sup>. To achieve this, we generated stable lines of MDCK cells (optoMDCK-Rac1) expressing two constructs: CIBN-GFP-CAAX and TIAM-CRY2-mCherry; the former is targeted to the plasma membrane, whereas the latter is cytosolic and carries the catalytic domain of Tiam1, an activator of Rac1. On illumination with blue light, the two constructs bind with high affinity, localizing Tiam1 at the membrane<sup>32,37,39-41</sup> (Fig. 1a). Previous work has shown that Rac1 is activated within the illuminated region<sup>37</sup>. As expected, photoactivated optoMDCK-Rac1 cells form a lamellipodium (Fig. 1b) and focal adhesions (Extended Data Fig. 1a).

To study the mechanical coupling of leaders and followers, we engineered minimalistic systems that captured fundamental elements of collective motion. We used microcontact printing on polyacrylamide gels of uniform stiffness (18 kPa) to create fibronectin-coated lines 20  $\mu m$  wide and several millimetres long. We seeded optoMDCK-Rac1 cells at a low concentration so that they attach to the lines either as single cells or in small linear groups ('cell trains') in media containing thymidine to halt cell division (Fig. 1c). Gels contained fluorescent microspheres so that traction force microscopy (TFM) could be performed  $^{42}$ .

We imaged regions containing cell trains ranging in length from one to four cells ( $N_c$  = 1–4; Fig. 1d). We performed an initial baseline measurement of 2 h without photoactivation, acquiring mCherry and microsphere fluorescence, and then photoactivated a subset of cell trains. To photoactivate trains, we illuminated one of their edges with blue light, inducing lamellipodia formation. The photoactivation and imaging continued for 4–5 h (Fig. 1e), and the photoactivation region was periodically moved following the train motion (Fig. 2a and Supplementary Videos 1–4). At the end of each experiment, cells were detached from the gel and an image of the relaxed microspheres was acquired for TFM calculations.

#### A photoactivated cell can only lead one follower

Before any analysis, we reoriented the images so that the photoactivated edge of the cell trains was always towards increasing coordinate y (Fig. 2a). We segmented and tracked both photoactivated and non-photoactivated cell trains and calculated V(t), their centre-of-mass velocity. As expected, regardless of the cell number  $N_c$ , the non-photoactivated cell trains have average velocities symmetrically distributed around 0, showing no preferred direction (Fig. 2b (bottom row) and Fig. 2c). In contrast, the velocities of the photoactivated cell trains with  $N_c$  = 1 are biased towards the direction of the photoactivated edge and generally have larger magnitudes than the corresponding non-photoactivated cases, confirming our ability to generate moving cells. Although cell trains with  $N_c$  = 2 also move significantly biased towards the photoactivated edge, this directional bias is lost for  $N_c \ge 3$ , with average velocities  $\langle V \rangle_t$  not significantly different between the photoactivated and non-photoactivated cell trains (Fig. 2b (top row) and Fig. 2c).

To investigate the impact of photoactivation beyond the centre-of-mass motion, for each train we separately analysed the sequences of instantaneous velocities of the top and bottom edges,  $v_+(t)$  and  $v_-(t)$ , respectively. We defined 'coherent motion' of a cell train as the case in which both top-edge and bottom-edge velocity medians,  $\tilde{v}_+$  and  $\tilde{v}_-$ , respectively, were significantly non-zero and had the same sign. We then termed 'directed motion' as the case of coherent motion in the direction of photoactivation ( $\tilde{v}_+ > 0$  and  $\tilde{v}_- > 0$ ; Fig. 2d). Conversely, we categorized the opposite case as 'antidirected motion' ( $\tilde{v}_+ < 0$  and  $\tilde{v}_- < 0$ ). The cases that did not exhibit coherent motion were termed spreading ( $\tilde{v}_+ > 0$  and  $\tilde{v}_- < 0$ ) and contraction ( $\tilde{v}_+ < 0$  and  $\tilde{v}_- > 0$ ).

By analysing all the photoactivated cell trains with this criterion, we found that a third of the single-cell trains exhibit directed motion, and no single cells are moving opposite to photoactivation (Fig. 2e). Consistent with our data on the centre-of-mass velocity, this effect is rapidly lost as  $N_c$  grows: the percentage of cell trains with directed motion decreases, and the percentage with antidirected motion increases (Fig. 2e). For  $N_c \ge 3$ , photoactivated cell trains behave comparably with non-photoactivated trains; there is no increase in directed motion due to photoactivation (Extended Data Fig. 2a).

We checked whether this behaviour was due to an inability of photoactivated cells to generate a lamellipodium when connected to more followers. To do so, we measured lamellipodium growth caused by photoactivation. We found that for all the values of  $N_c$ , the photoactivated trains display significant increases in lamellipodium size, and that this increase does not depend on  $N_c$  (Extended Data Fig. 1b,c). Moreover, the percentage of photoactivated top edges where  $\tilde{\nu}_+$  is significantly larger than 0 is >50% for all the values of  $N_c$  (Extended Data Fig. 2b), supporting the fact that photoactivation induces protrusion formation for all the train lengths. We also tested whether the response of cell trains to photoactivation was influenced by their behaviour before photoactivation. We found that nearly all the trains that undergo coherent motion after photoactivation were initially either spreading or contracting, indicating that no directedness existed before photoactivation (Extended Data Fig. 3).

Taken together, our experiments show that the induced leader cells are not capable of driving coherent motion of more than one follower.

## Coherent motion requires asymmetric traction and tension fields

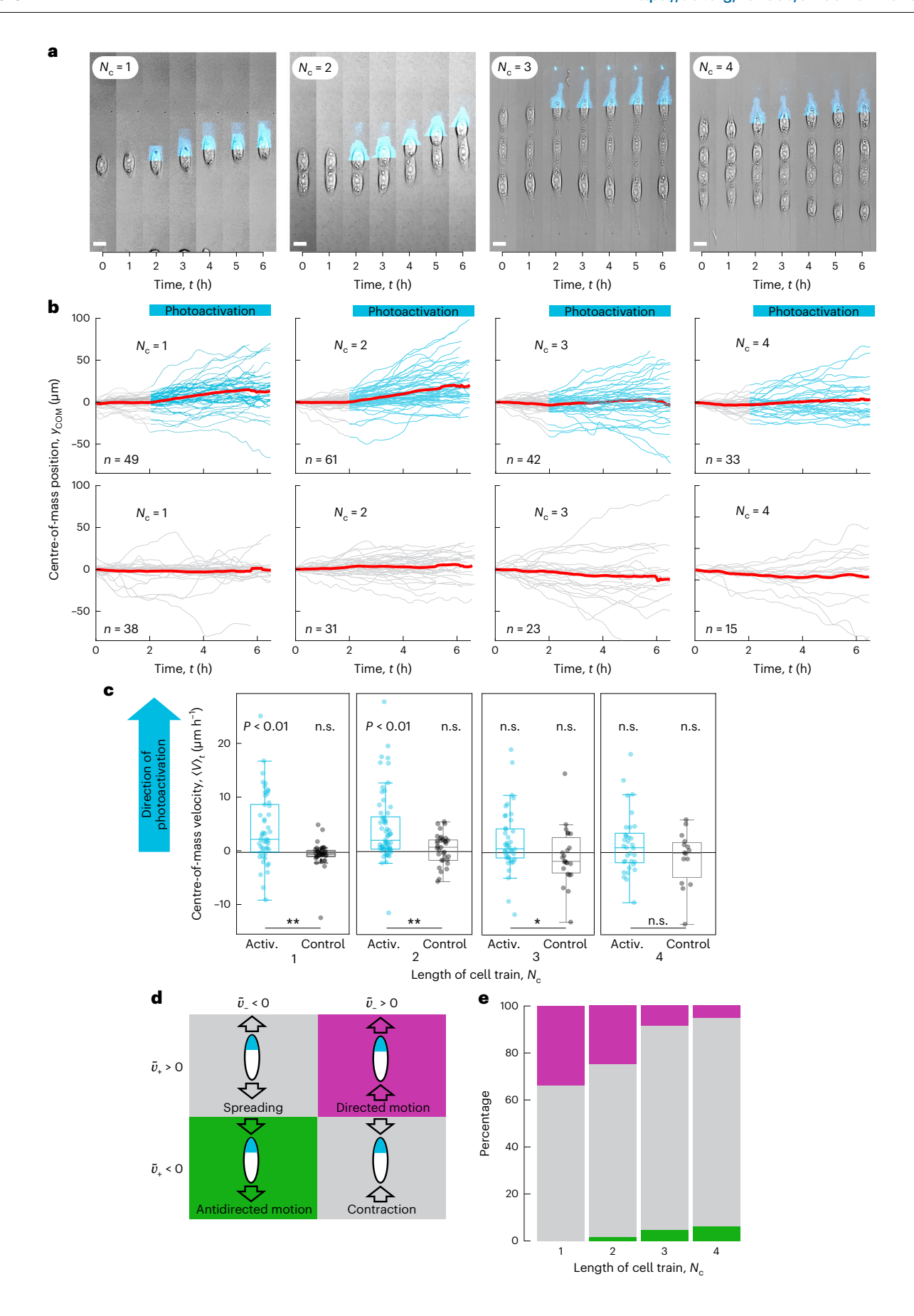
To identify the determinants of coherent group motion, we study the longitudinal traction forces  $T_y$  exerted by the cells on the substrate (Fig. 3a,b). As expected, for  $N_c$  = 1, cell tractions form a contractile dipole (Fig. 3b). Longer cell trains exhibit more complex patterns that are not simple superpositions of  $N_c$  dipoles, indicating that the cells in a train are not mechanically independent (Fig. 3b,c).

For different train lengths  $N_c$ , we computed the profile  $\langle T_y \rangle_{x,t}$  averaged over the train width x and time t. We compared these profiles

#### Fig. 2 | Leader cell migratory efficiency decreases with number of followers.

**a**, Representative cell trains during the photoactivation of a cell edge. Scale bars,  $20 \, \mu m$ . **b**, Centre-of-mass trajectories for all the cell trains. The top row shows the photoactivated trains, and the blue curves represent the duration of photoactivation. The bottom row shows the control trains. The red lines are the average trajectories. **c**, Average migration velocities of the centre of mass of all the photoactivated and control cell trains. Statistical significance quantified by a two-sided Wilcoxon rank-sum test. For the two-sample tests, \*\* indicates P < 0.01 and \* indicates P < 0.05. Box plots show the first quartile, median and third quartile. Range includes all the data points. Whiskers extend to the first

adjacent value within the 1.5× interquartile range. Full P values are listed in Supplementary Table 1.  $\mathbf{d}$ , Types of cell train migration based on the motion of the top and bottom edges.  $\mathbf{e}$ , Motion of photoactivated cell trains according to the definitions in  $\mathbf{d}$ . Magenta represents the percentage of trains that undergo collective migration in the direction of photoactivation (that is, directed migration), and green is in the opposite direction (antidirected migration). Percentages of directed migration are 32.6% ( $N_c$  = 1), 27.9% ( $N_c$  = 2), 9.5% ( $N_c$  = 3) and 6.0% ( $N_c$  = 4); the total sample sizes are n = 49, n = 61, n = 42 and n = 33, respectively. n = 292 cell trains examined over 59 independent experiments.



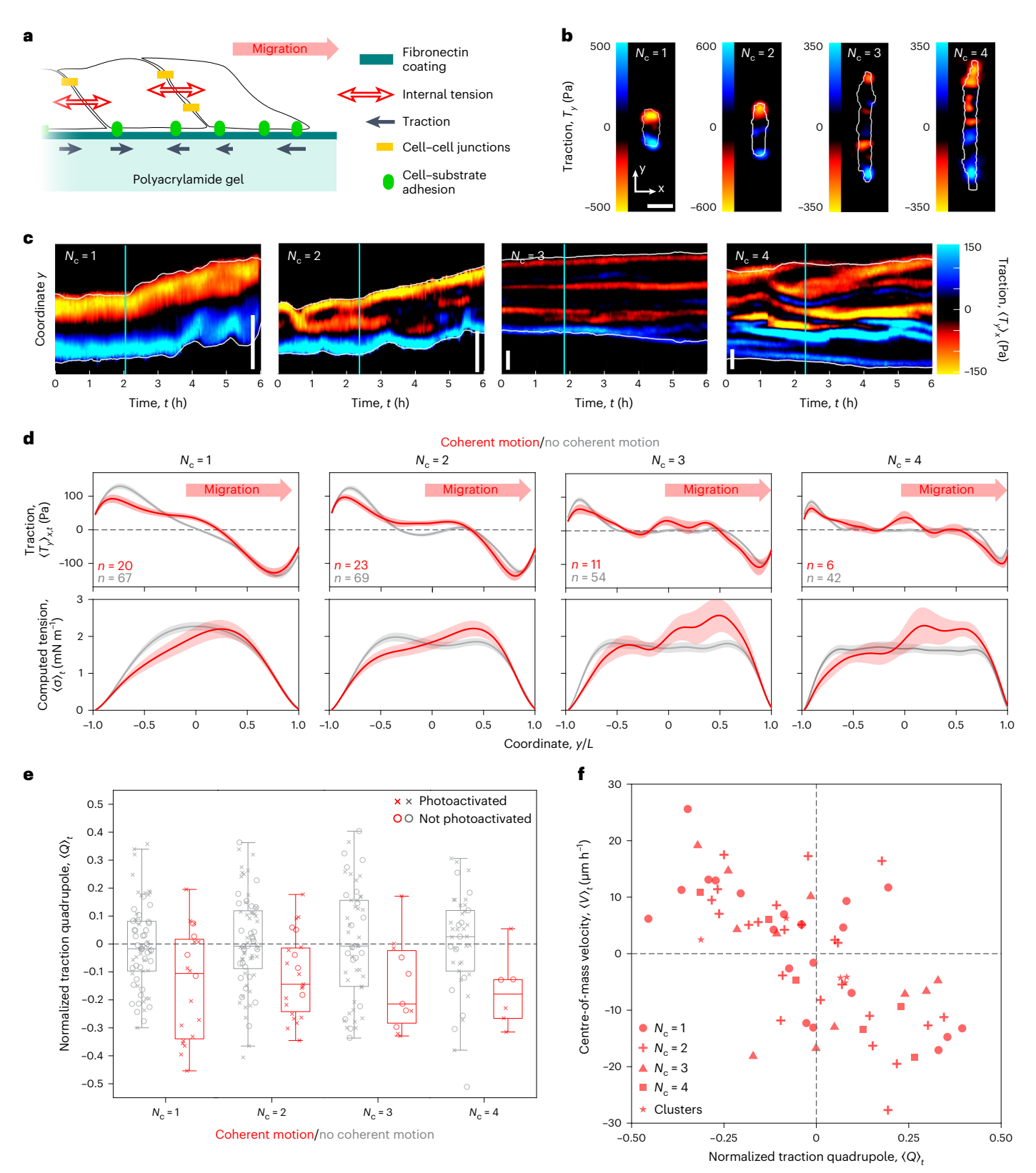


**Fig. 3** | **Asymmetric traction and tension profiles drive the migration of cell trains. a**, Scheme of cell–substrate traction and tension within a cell train. **b**, Representative fields of longitudinal traction forces for trains of different lengths. **c**, Representative kymographs of the longitudinal tractions. The cyan lines mark the beginning of the photoactivation intervals, and the white lines are the cell edges. Scale bars, 50 µm. **d**, Average profiles of the longitudinal component of the traction forces (top row) and of internal tension (bottom row), for cell trains undergoing coherent motion (red) and for other trains (grey). The shaded regions along the curves show the standard error of the mean. Averages are over different

cell trains; number of cell trains n is indicated on the plot.  $\mathbf{e}$ , Normalized traction quadrupole of trains exhibiting coherent movement (red) and other trains (grey). Box plots show the first quartile, median and third quartile. Range includes all the data points. Whiskers extend to the first adjacent value within the 1.5× interquartile range. P values are listed in Supplementary Table 1.  $\mathbf{f}$ , Scatter plot of the average centre-of-mass velocity and normalized traction quadrupole in the cell trains and clusters (Fig. 4) exhibiting coherent motion. R = 0.66, P < 0.01. For clarity, in this plot, the cell train velocities have not been aligned with the positive axis. n = 292 cell trains examined over 59 independent experiments.

between cell trains that did and did not move coherently. Our data show that coherent motion occurs both in photoactivated trains (Fig. 2e) and, with a lower probability, in non-photoactivated ones (Extended Data Fig. 2a). Therefore, we binned our data in two groups, one of all non-coherently moving trains and another one of all coherently moving trains, regardless of whether the coherent motion was directed or antidirected and whether the trains were photoactivated or non-photoactivated (Extended Data Fig. 4 shows the different groupings of these data). To compare the moving trains regardless of their direction of motion, we aligned the profiles with y > 0 in the direction of coherent motion.

The average traction profiles of trains that do not move coherently are symmetric, with tractions of equal magnitude concentrated at the train edges (Fig. 3d (top row), grey curves). With increasing train length, the tractions in the central region vanish, meaning that although the edge tractions are sustained in time, central tractions are transient and tend to cancel out. By contrast, in trains undergoing coherent movement,  $\langle T_y \rangle_{x,t}$  becomes asymmetric; the tractions at the trailing edge are lower in magnitude and extend further into the train, even reaching the central region (Fig. 3d (top row), red curves).

To quantify this mechanical asymmetry, we computed the time-averaged one-dimensional (1D) normalized traction quadrupole  $Q = (\int T_y y^2 \mathrm{d}y)/(\int |T_y|y^2 \mathrm{d}y)$ , which is the normalized second moment of the traction field along the train axis with respect to the centre of mass <sup>43–46</sup>. Since we are considering the coherent motion of all the trains as being towards positive y, the quadrupole Q is negative for traction profiles like those of the trains undergoing coherent movement. Indeed, we found that in nearly all the trains undergoing coherent movement  $\langle Q \rangle_t$  is negative, whereas in other trains it takes positive and negative values with equal probability (Fig. 3e).

We then studied the distribution of internal tension within the cell trains by calculating  $\sigma$ , the tension transmitted inside the cells by the cytoskeleton and between cells by cell–cell junctions. The internal tension balances the tractions at the cell–substrate interface and in a 1D system it is given by  $\sigma(y,t) = \int_{-L}^{y} T_y(y^*,t) \, dy^*$ , where 2L is the length of the cell train<sup>29</sup>. Analogous to our calculation of  $\langle T_y \rangle_{x,t}$ , we computed the ensemble averages of  $\sigma$ . We found that trains that do not exhibit coherent movement have symmetric average tension profiles, whereas the trains that move coherently have an asymmetric tension profile with a broad peak located closer to the leading edge (Fig. 3d, bottom row).

We then wondered if the value of  $\langle Q \rangle_t$  was related to the centre-of-mass velocity  $\langle V \rangle_t$ . In Fig. 3a-e, we aligned all the data so that the coherent motion of trains was in the direction of increasing y. Now, however, to better visualize the relationship between velocity and traction asymmetry, we went back to considering trains moving with either positive or negative velocity, as they occurred in the experiments. Strikingly, for all the trains exhibiting coherent motion,  $\langle V \rangle_t$  and  $\langle Q \rangle_t$  are correlated. Faster trains have stronger traction asymmetries, resulting in tension that is more concentrated towards their leading edge (Fig. 3f).

Taken together, these results show that train movement is driven by the global spatial distribution of mechanical stress. Front-back asymmetries along the train are necessary for coherent motion, and stronger asymmetries drive faster motion.

#### Migrating 2D clusters and monolayer fingers

The directed migration of 1D cell trains is common in processes such as angiogenesis<sup>47</sup>, branching morphogenesis<sup>48</sup> and collective cancer invasion through interstitial spaces<sup>49</sup>. In many other processes, cells migrate as either two-dimensional (2D) clusters or multicellular protrusions from a cell sheet<sup>23</sup>. We, thus, asked whether the mechanical asymmetries observed in migrating 1D cell trains are also present in these 2D systems.

To this end, we patterned wider fibronectin lines ( $50 \mu m \arccos$ ) and seeded optoMDCK-Rac1 cells, obtaining clusters that are 2–3 cells wide (Fig. 4a–c). We selected clusters of 5–15 cells and photoactivated

their top edge, applying the same experimental protocol and analysis used for the cell trains (Supplementary Video 5). Similar to longer trains, only a small fraction of clusters migrated coherently (-11%). We then computed the time-averaged traction profile  $\langle T_y \rangle_{x,t}$  for clusters that did not move coherently and for those that did. Like in cell trains, the traction profile of the non-coherently moving clusters is symmetric (Fig. 4e, grey curves). By contrast, in coherently moving clusters, tractions at the leading edge are higher in magnitude and those at the trailing edge extend further into the cluster (Fig. 4e, red curves). Accordingly, in these clusters, tension has an asymmetric profile with higher values towards the leading edge (Fig. 4g). Plotting the values of  $\langle V \rangle_t$  and  $\langle Q \rangle_t$  for the migrating clusters (Fig. 3f), we found that they behave similarly to the cell trains.

Next, we looked at multicellular finger-like protrusions at the edge of an expanding epithelial monolayer in which the traction forces generated by several MDCK fingers were measured using micropillars<sup>23</sup>. We analysed the component of tractions along the finger's axis, averaged across the width of the finger analogous to how we previously calculated  $\langle T_y \rangle_{x,t}$  (Fig. 4d). The resulting average traction profile shows an asymmetry similar to coherently moving trains and clusters: tractions are higher and more localized at the leading edge than at the trailing edge (Fig. 4f). This profile results in an asymmetric tension with higher values towards the front (Fig. 4h). These findings suggest that the relationship between collective cell migration and tension asymmetries is a general principle that applies to both 1D and 2D systems.

## An active fluid model explains the force-velocity relation

So far, our results show that an autonomous leader cell is not sufficient to drive coherent group motion. We instead find that coherent motion requires a supracellular traction and tension asymmetry, and that this asymmetry correlates with the migration velocity. To understand how tension distributions drive collective migration, we modelled a cell train as a 1D compressible active fluid that exerts tractions on the substrate so. Force balance reads  $\partial_{\nu}\sigma = T$ , where  $\sigma = \eta \partial_{\nu}v$  is the internal tension,  $\eta$  is the effective viscosity and v is the velocity field. Here, T is the total traction that results from viscous drag  $\xi v$  on the substrate, and from myosin-generated forces termed as active tractions  $T_a$ . Thus, the total traction is

$$T = \xi v - T_{\rm a},\tag{1}$$

and the force balance is given by

$$\eta \partial_{\nu}^2 v = \xi v - T_a. \tag{2}$$

When a cell polarizes, it develops spatial asymmetries in force generation. To study how these asymmetries drive motion, we took an active traction profile given by

$$T_{a}(y) = \begin{cases} \zeta_{+} \frac{\sinh(y/\ell_{+})}{\sinh(L/\ell_{+})}; y \ge 0\\ \zeta_{-} \frac{\sinh(y/\ell_{-})}{\sinh(L/\ell_{-})}; y < 0, \end{cases}$$
(3)

where 2L is the train length. Equation (3) generalizes the active traction profiles in previous models<sup>50–53</sup> to now account for spatial asymmetries in both their magnitude  $\zeta_{\pm}$  at the train edges and their decay length  $\ell_{\pm}$  towards the train interior (Fig. 5a).

To analyse how these two sources of asymmetry shape the total traction and tension profiles, we calculated the centre-of-mass velocity  $V=\frac{1}{2L}\int_{-L}^{L}v\left(y\right)\mathrm{d}y$ . Averaging equation (2) over y and imposing stress-free boundary conditions  $[\sigma(-L)=\sigma(L)=0]$ , we obtained

$$V = \frac{1}{2L\xi} \int_{-L}^{L} T_{a}(y) dy = \frac{1}{2L\xi} \left[ \zeta_{+} \ell_{+} \tanh \left( \frac{L}{2\ell_{+}} \right) - \zeta_{-} \ell_{-} \tanh \left( \frac{L}{2\ell_{-}} \right) \right]. \tag{4}$$

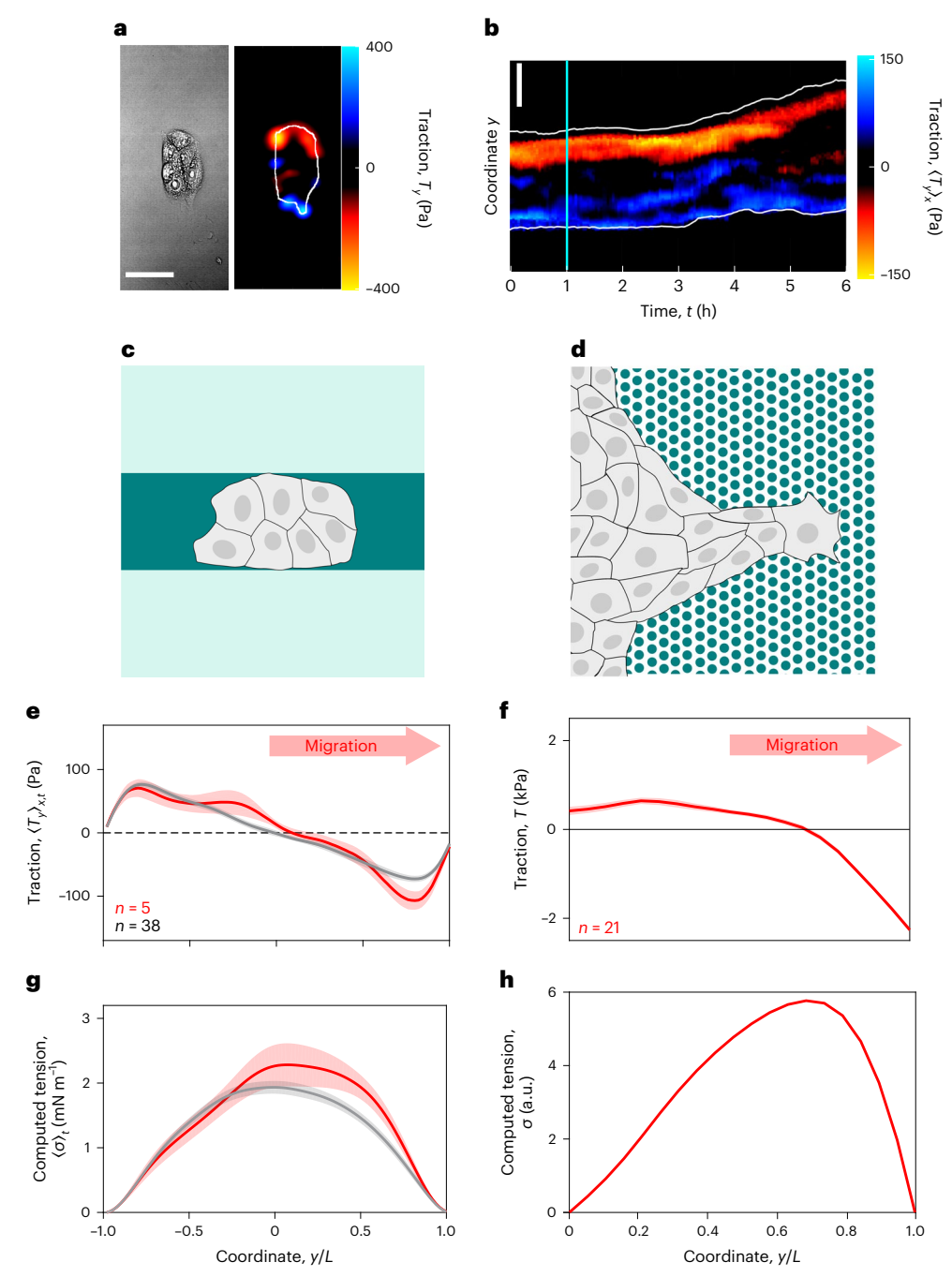


**Fig. 4** | **Asymmetric traction profiles in 2D cell groups. a**, Phase contrast image and longitudinal traction forces of a cell island. Scale bar, 50 μm. Representative data from n = 43 islands examined over eight independent experiments. **b**, Kymograph of longitudinal tractions. The cyan lines mark the beginning of the photoactivation intervals. Scale bar, 50 μm. **c**, Diagram of a cell island on a micropatterned fibronectin line (dark green) on a polyacrylamide gel (light green). **d**, Diagram of a migrating finger from a monolayer edge on pillars. **e**, Average profiles of the longitudinal component of the traction forces, for cell islands undergoing coherent motion (red) and for other trains (grey).

The shaded regions represent the standard error. Averages are over different cell islands; number of cell trains  $\boldsymbol{n}$  is indicated on the plot.  $\boldsymbol{f}$ , Average profile of the longitudinal component of the traction forces, for migrating cell fingers. The shaded region represents the standard error of the mean. Averages are over different cell fingers; their number  $\boldsymbol{n}$  is indicated on the plot.  $\boldsymbol{g}$ , Average profiles of the computed tension for cell islands undergoing coherent motion (red) and for other trains (grey). The shaded regions represent the standard error of the mean.  $\boldsymbol{h}$ , Average profiles of the computed tension for migrating cell fingers.

Equation (4) shows that the integral of active traction drives cluster motion. This result provides an explicit force–velocity relation for a cell cluster, linking its motion to the asymmetries in the underlying active traction field.

Then, solving equation (2) with stress-free boundary conditions as well as velocity and stress continuity at y=0, we obtained the velocity profile v(y) and used it to calculate the total traction quadrupole, that is,  $Q=\int_{-L}^L T(y)y^2 \mathrm{d}y$ , in terms of  $\zeta_+$ ,  $\zeta_-$ ,  $\ell_+$ ,  $\ell_-$  and the screening length

 $\lambda = \sqrt{\eta/\xi}$  (Supplementary Notes A and B). Figure 5b summarizes, in a 2D diagram, how the signs of velocity and quadrupole change with the asymmetry ratios  $\zeta_*/\zeta_-$  and  $\ell_*/\ell_-$ . Below, we illustrate these results by following the paths indicated by the pink, green and blue arrows. The profiles of all the fields at the points along these paths are shown in Fig. 5c-n, and the variation in velocity and quadrupole along the green and blue paths are plotted in Fig. 5o-q.

First, keeping the decay lengths equal, that is,  $\ell_+ = \ell_-$ , we varied the ratio between the magnitude of active traction at the train edges, namely,  $\zeta_+/\zeta_-$  (Fig. 5b, pink arrow). In the symmetric case ( $\zeta_+/\zeta_- = 1$ ), there is no possibility for net motion, as the train protrudes with equal force in both directions. As we increase  $\zeta_+/\zeta_-$ , making the active traction relatively stronger on the right (Fig. 5c), the train moves to the right (Fig. 5d, positive velocity). The profiles of total traction have an asymmetry analogous to those of active traction (Fig. 5e), which gives negative quadrupoles (Q < 0; Fig. 5b, pink). Accordingly, the tension is concentrated towards the front (Fig. 5f) and the centre-of-mass velocity is positive and increases with the asymmetry (Fig. 5d, averages of profiles).

Next, we varied the ratio between the decay length of active traction on each side of the train  $(\ell_+/\ell_-)$  while keeping the magnitudes equal (Fig. 5b, green arrow). Starting again from the symmetric case, we now decreased  $\ell_+/\ell_-$ , which makes the active traction more localized on the right edge (Fig. 5g). Now, the total traction and tension profiles shift towards the left, which gives a positive quadrupole (Q > 0) and drives leftwards migration (V < 0) (Fig. 5h–j and Fig. 5b, green).

In the two cases above, V has the opposite sign of Q and its magnitude increases with that of Q (Fig. 50–q, green lines), consistent with our experimental results (Fig. 3e,f). Our theory also predicts additional scenarios in which the two sources of spatial asymmetries (magnitude versus localization) in active traction have competing effects on cell motion (Supplementary Note C). In these cases, there are parameter regions in which V and Q have the same sign (Fig. 5b (blue path) illustrated in Fig. 5k–n), even if the magnitude of V always increases with that of Q (Fig. 50–q, blue curves).

So far, our model assumed that friction was uniform. We generalized the model to account for a non-uniform friction coefficient with the same profile as active traction (Supplementary Note D), which could result from a non-uniform distribution of focal adhesions<sup>54</sup>. The velocity, tension and traction profiles are only slightly modified with respect to the case with uniform friction coefficient (Extended Data Fig. 5), showing that our conclusions also hold in the presence of a non-uniform friction coefficient.

#### Fitting theory to experiments

Next, we fitted the model to the experimental traction profiles (Fig. 3d), and we extracted the values of the active traction parameters  $\zeta_+$ ,  $\zeta_-$ ,  $\ell_+$ ,  $\ell_-$  and friction term  $\xi V$  (Extended Data Fig. 6), which positioned the cell trains of different lengths in the model parameter space (Fig. 5r). As expected, cell trains with no coherent motion fall at the origin of the diagram (1, 1), reflecting the symmetry in traction profiles. By contrast, cell trains displaying coherent motion fall in the top-right-hand quadrant (Q < 0 and V > 0), indicating an asymmetry in both traction magnitude and decay length.

the diagram (1,1), reflecting the symmetry in traction profiles. By co trast, cell trains displaying coherent motion fall in the top-right-har quadrant (Q < 0 and V > 0), indicating an asymmetry in both traction magnitude and decay length.

Fig. 5 | An active polar fluid model explains how traction asymmetries drive migration. a, Scheme of a cell train (grey) that exerts an asymmetric active traction profile (dark blue curve) on the substrate (light blue). b, Diagram showing the signs of the centre-of-mass velocity V and the traction quadrupole Q as a function of asymmetries in traction magnitude and decay length. The colour-coded points and arrows correspond to the parameter values used for the profiles in  $\mathbf{c}$ - $\mathbf{n}$ . All the panels are plotted for  $\ell_- = 0.4L$  and  $\lambda = 10L$ , where 2L is the train length. We chose  $\lambda \gg L$  to ensure tension transmission across the entire cell train  $^{52,71}$ .  $\mathbf{c}$ - $\mathbf{n}$ , Illustrative results of the model in different regimes of asymmetries of the active tractions. The columns correspond to profiles of

different quantities. The rows with pink, green and blue frames correspond to

the paths indicated by the corresponding arrows in **b. c-f**, Decreasing active

traction magnitude at the left edge (c) results in increased cell velocity (d), as

well as in asymmetric total tractions (e) and tension concentrated to the right

results in negative velocity (h), as well as asymmetric tractions (i) and tension

decay length of active tractions. As the active tractions become more localized

(f).  $\mathbf{g}$ - $\mathbf{j}$ , Decreasing the decay length of active tractions at the right edge ( $\mathbf{g}$ )

concentrated towards the left (j). k-n, Asymmetry in both magnitude and

Finally, we used our model to recapitulate the experimental relationship between traction quadrupole and velocity (Fig. 3f). We fitted the traction profiles of all the individual cell trains and obtained the probability distributions of parameter values  $\zeta_+$ ,  $\zeta_-$ ,  $\ell_+$ ,  $\ell_-$  and  $\xi$ . From these distributions, we generated a set of 60 simulated cell trains, for which we calculated the traction quadrupole Q and used equation (4) to compute V. We then plotted V against Q (Fig. 5s) and obtained a correlation analogous to the experimental relationship between  $\langle V \rangle_t$  and  $\langle Q \rangle_t$  (Fig. 3f).

Overall, our theory provides a force–velocity relation for collective cell migration (equation (4)) and captures the link between motion and strength of the mechanical asymmetries in cell clusters quantified by the traction quadrupole (Fig. 5q). Beyond capturing our experimental measurements (Figs. 3f and 5r,s), our theory reveals that the velocity–quadrupole relation depends on the interplay between asymmetries in the magnitude and localization of cellular forces, providing quantitative predictions for future experiments.

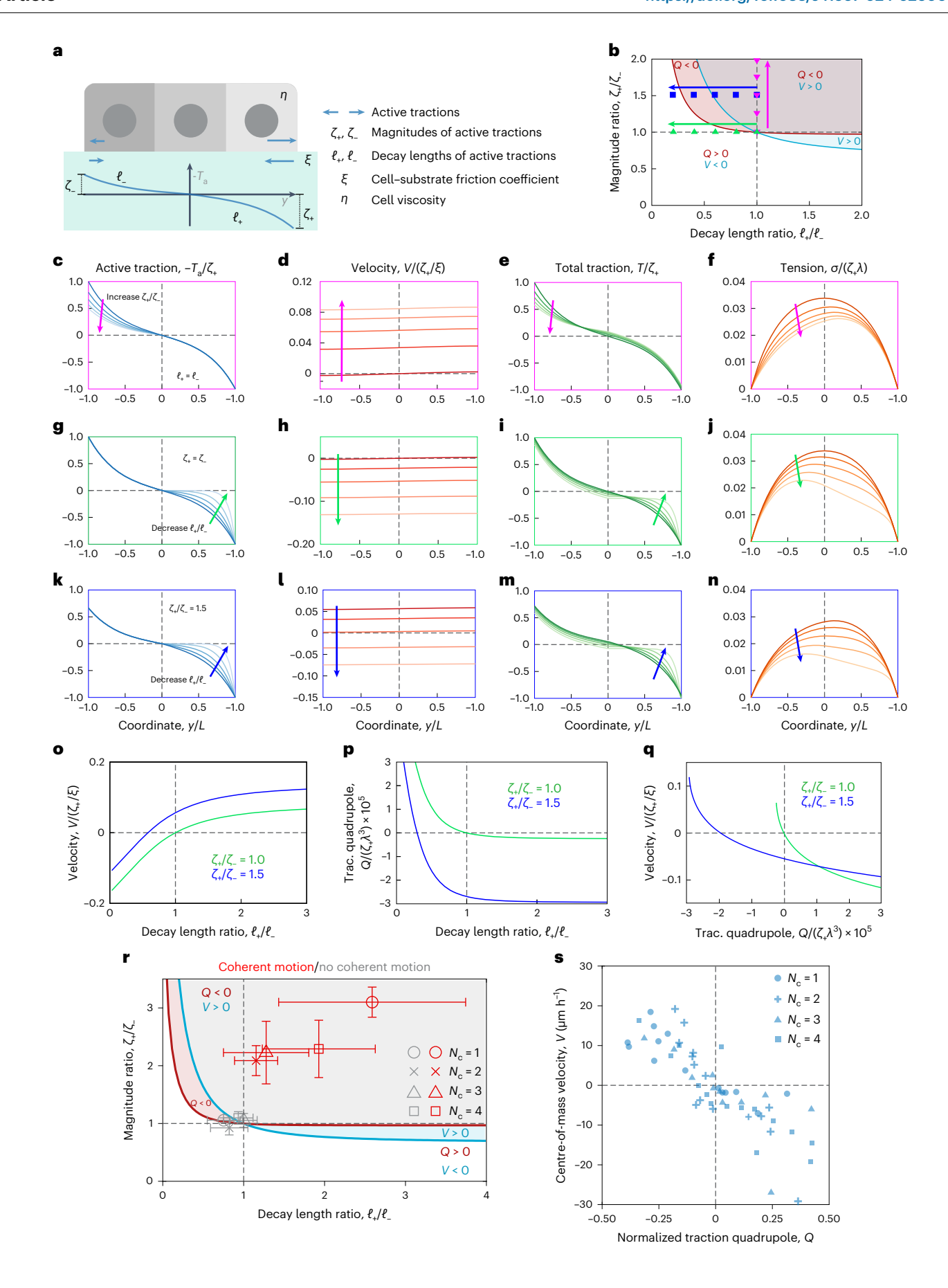
#### **Discussion**

We investigated how cell groups undergo coherent motion. Using optogenetics, we tested if a single protrusive cell could guide an entire group. We found that a leader cell cannot guide more than one follower. Through the measurement of cellular forces and theoretical modelling, we showed that collective cell migration requires a global asymmetry in the tension profile within the cell cluster. Leaders need the followers' contributions to this asymmetry for effective guidance.

The relation between cellular forces and velocities is a fundamental and unresolved problem in cell migration 46,55-59. Because inertia and viscous drag against the surrounding fluid are negligible, the sum of tractions exerted by cells on the substrate is always zero and therefore is not indicative of the magnitude or direction of cell velocity. Previous work at the single-cell level established that asymmetries in the traction distribution correlate with the direction of cell movement 43,45. However, a general quantitative relationship between force and velocity was lacking at both single-cell and collective cell levels 43,45,59-64. Here we showed that cluster velocity increases with global stress asymmetry. To understand the origin of this relationship, we modelled the cluster as a 1D active polar fluid that can generate asymmetric active tractions. This model fits the experimental total traction and tension distributions, and it reproduces the relationship between tension asymmetry and cell velocity.

Since leader activation alone cannot guide large groups, our study raises the question of how leaders and followers organize to form the asymmetry needed for collective migration. Communication might involve patterns in cell differentiation, paracrine signalling or direct cell contact  $^{65-70}$ . In uncontrolled scenarios like cancer invasion, asymmetry

at the right edge (k), velocity decreases in magnitude and eventually changes sign (1). The total tractions (m) and tension (n) profiles also shift from being right-concentrated to left-concentrated, corresponding to a change in sign of the traction quadrupole Q. o,p, Centre-of-mass velocity (o) and traction  $quadrupole(\mathbf{p})$  as a function of the decay length asymmetry of active tractions. The colours correspond to the parameter paths indicated by arrows in **b**. **q**, Velocity as a function of the quadrupole obtained by varying the decay length ratio. The velocity and quadrupole simultaneously change sign only when the active traction magnitude is symmetric (green). **r**, Diagram as that in **b**, showing the values of active traction magnitude and decay length ratios obtained from the fits to the experimental profiles in Fig. 3d. Coherently moving cell trains (red points) fall in the region with positive velocity and negative quadrupole (V > 0, Q < 0), whereas non-coherently moving cell trains (grey points) have symmetric traction profiles that fall close to the origin at (1, 1). The error bars are confidence intervals derived from fits (Methods). s, Model simulations recapitulating the data in Fig. 3f. Points are calculated from 60 sets of parameter values  $\zeta_+, \zeta_-, \ell_+, \ell_$ and  $\xi$  drawn from the probability distributions obtained from fits of the model to all the individual cell trains (Methods).



might arise stochastically, as we observed when some groups migrated even without photoactivation (Fig. 3). By defining the mechanical rules of leadership, we set an experimental and conceptual basis to test these communication mechanisms.

#### Online content

Any methods, additional references, Nature Portfolio reporting summaries, source data, extended data, supplementary information, acknowledgements, peer review information; details of author contributions and competing interests; and statements of data and code availability are available at https://doi.org/10.1038/s41567-024-02600-2.

#### References

- Schaller, V., Weber, C., Semmrich, C., Frey, E. & Bausch, A. R. Polar patterns of driven filaments. *Nature* 467, 73–77 (2010).
- Boudet, J. F. et al. From collections of independent, mindless robots to flexible, mobile, and directional superstructures. Sci. Robot. 6, eabd0272 (2021).
- Silverberg, J. L., Bierbaum, M., Sethna, J. P. & Cohen, I. Collective motion of humans in mosh and circle pits at heavy metal concerts. *Phys. Rev. Lett.* 110, 228701 (2013).
- Suzuki, R., Weber, C. A., Frey, E. & Bausch, A. R. Polar pattern formation in driven filament systems requires non-binary particle collisions. *Nat. Phys.* 11, 839–843 (2015).
- Ben-Jacob, E., Cohen, I. & Levine, H. Cooperative self-organization of microorganisms. Adv. Phys. 49, 395–554 (2000).
- Gómez-Nava, L., Bon, R. & Peruani, F. Intermittent collective motion in sheep results from alternating the role of leader and follower. Nat. Phys. 18, 1494–1501 (2022).
- Yllanes, D., Leoni, M. & Marchetti, M. C. How many dissenters does it take to disorder a flock? New J. Phys. 19, 103026 (2017).
- Pearce, D. J. G. & Giomi, L. Linear response to leadership, effective temperature, and decision making in flocks. *Phys. Rev. E* 94, 022612 (2016).
- Pinkoviezky, I., Couzin, I. D. & Gov, N. S. Collective conflict resolution in groups on the move. *Phys. Rev. E* 97, 032304 (2018).
- Couzin, I. D., Krause, J., Franks, N. R. & Levin, S. A. Effective leadership and decision-making in animal groups on the move. *Nature* 433, 513–516 (2005).
- Nagy, M., Ákos, Z., Biro, D. & Vicsek, T. Hierarchical group dynamics in pigeon flocks. *Nature* 464, 890–893 (2010).
- Omelchenko, T., Vasiliev, J. M., Gelfand, I. M., Feder, H. H. & Bonder, E. M. Rho-dependent formation of epithelial 'leader' cells during wound healing. *Proc. Natl Acad. Sci. USA* 100, 10788–10793 (2003).
- Poujade, M. et al. Collective migration of an epithelial monolayer in response to a model wound. *Proc. Natl Acad. Sci. USA* **104**, 15988–15993 (2007).
- Khalil, A. A. & Friedl, P. Determinants of leader cells in collective cell migration. *Integr. Biol.* 2, 568 (2010).
- Mayor, R. & Etienne-Manneville, S. The front and rear of collective cell migration. Nat. Rev. Mol. Cell Biol. 17, 97–109 (2016).
- Theveneau, E. & Linker, C. Leaders in collective migration: are front cells really endowed with a particular set of skills? F1000Res. 6, 1899 (2017).
- 17. Yang, Y. & Levine, H. Leader-cell-driven epithelial sheet fingering. *Phys. Biol.* **17**, 046003 (2020).
- Pinheiro, D., Kardos, R., Hannezo, É. & Heisenberg, C.-P. Morphogen gradient orchestrates pattern-preserving tissue morphogenesis via motility-driven unjamming. *Nat. Phys.* 18, 1482–1493 (2022).
- Camley, B. A. & Rappel, W.-J. Physical models of collective cell motility: from cell to tissue. J. Phys. Appl. Phys. 50, 113002 (2017).

- Martinson, W. D. et al. Dynamic fibronectin assembly and remodeling by leader neural crest cells prevents jamming in collective cell migration. *eLife* 12, e83792 (2023).
- 21. Kozyrska, K. et al. p53 directs leader cell behavior, migration, and clearance during epithelial repair. Science **375**, eabl8876 (2022).
- 22. Yamaguchi, N., Mizutani, T., Kawabata, K. & Haga, H. Leader cells regulate collective cell migration via Rac activation in the downstream signaling of integrin β1 and PI3K. Sci. Rep. **5**, 7656 (2015).
- Reffay, M. et al. Interplay of RhoA and mechanical forces in collective cell migration driven by leader cells. *Nat. Cell Biol.* 16, 217–223 (2014).
- Hino, N. et al. A feedback loop between lamellipodial extension and HGF-ERK signaling specifies leader cells during collective cell migration. Dev. Cell 57, 2290–2304.e7 (2022).
- 25. Vishwakarma, M. et al. Mechanical interactions among followers determine the emergence of leaders in migrating epithelial cell collectives. *Nat. Commun.* **9**, 3469 (2018).
- Law, R. A. et al. Cytokinesis machinery promotes cell dissociation from collectively migrating strands in confinement. Sci. Adv. 9, eabq6480 (2023).
- Cai, D. et al. Mechanical feedback through E-cadherin promotes direction sensing during collective cell migration. Cell 157, 1146–1159 (2014).
- 28. Vishwakarma, M., Spatz, J. P. & Das, T. Mechanobiology of leader-follower dynamics in epithelial cell migration. *Curr. Opin. Cell Biol.* **66**, 97–103 (2020).
- 29. Trepat, X. et al. Physical forces during collective cell migration. *Nat. Phys.* **5**, 426–430 (2009).
- Caussinus, E., Colombelli, J. & Affolter, M. Tip-cell migration controls stalk-cell intercalation during *Drosophila* tracheal tube elongation. *Curr. Biol.* 18, 1727–1734 (2008).
- 31. Arima, S. et al. Angiogenic morphogenesis driven by dynamic and heterogeneous collective endothelial cell movement. *Development* **138**, 4763–4776 (2011).
- 32. Wang, X., He, L., Wu, Y. I., Hahn, K. M. & Montell, D. J. Light-mediated activation reveals a key role for Rac in collective guidance of cell movement in vivo. *Nat. Cell Biol.* **12**, 591–597 (2010).
- Labernadie, A. et al. A mechanically active heterotypic E-cadherin/N-cadherin adhesion enables fibroblasts to drive cancer cell invasion. *Nat. Cell Biol.* 19, 224–237 (2017).
- Cheung, K. J., Gabrielson, E., Werb, Z. & Ewald, A. J. Collective invasion in breast cancer requires a conserved basal epithelial program. Cell 155, 1639–1651 (2013).
- 35. Vilchez Mercedes, S. A. et al. Decoding leader cells in collective cancer invasion. *Nat. Rev. Cancer* **21**, 592–604 (2021).
- Machacek, M. et al. Coordination of Rho GTPase activities during cell protrusion. *Nature* 461, 99–103 (2009).
- 37. de Beco, S. et al. Optogenetic dissection of Rac1 and Cdc42 gradient shaping. *Nat. Commun.* **9**, 4816 (2018).
- 38. Drozdowski, O. M., Ziebert, F. & Schwarz, U. S. Optogenetic control of migration of contractile cells predicted by an active gel model. *Commun. Phys.* **6**, 158 (2023).
- 39. Valon, L. et al. Predictive spatiotemporal manipulation of signaling perturbations using optogenetics. *Biophys. J.* **109**, 1785–1797 (2015).
- Kennedy, M. J. et al. Rapid blue-light-mediated induction of protein interactions in living cells. *Nat. Methods* 7, 973–975 (2010).
- 41. Valon, L., Marín-Llauradó, A., Wyatt, T., Charras, G. & Trepat, X. Optogenetic control of cellular forces and mechanotransduction. *Nat. Commun.* **8**, 14396 (2017).
- Roca-Cusachs, P., Conte, V. & Trepat, X. Quantifying forces in cell biology. Nat. Cell Biol. 19, 742–751 (2017).

- Hennig, K. et al. Stick-slip dynamics of cell adhesion triggers spontaneous symmetry breaking and directional migration of mesenchymal cells on one-dimensional lines. Sci. Adv. 6, eaau5670 (2020).
- Butler, J. P., Tolić-Nørrelykke, I. M., Fabry, B. & Fredberg, J. J. Traction fields, moments, and strain energy that cells exert on their surroundings. Am. J. Physiol. Cell Physiol. 282, C595–C605 (2002).
- Tanimoto, H. & Sano, M. A simple force-motion relation for migrating cells revealed by multipole analysis of traction stress. *Biophys. J.* 106, 16–25 (2014).
- Delanoë-Ayari, H., Rieu, J. P. & Sano, M. 4D traction force microscopy reveals asymmetric cortical forces in migrating *Dictyostelium* cells. *Phys. Rev. Lett.* **105**, 248103 (2010).
- Costa, G. et al. Asymmetric division coordinates collective cell migration in angiogenesis. Nat. Cell Biol. 18, 1292–1301 (2016).
- 48. Hayashi, S. & Dong, B. Shape and geometry control of the Drosophila tracheal tubule. Dev. Growth Differ. **59**, 4-11 (2017).
- 49. Weigelin, B., Bakker, G.-J. & Friedl, P. Intravital third harmonic generation microscopy of collective melanoma cell invasion. *IntraVital* **1**, 32–43 (2012).
- Alert, R. & Trepat, X. Physical models of collective cell migration.
   Annu. Rev. Condens. Matter Phys. 11, 77–101 (2020).
- 51. Pérez-González, C. et al. Active wetting of epithelial tissues. *Nat. Phys.* **15**, 79–88 (2019).
- Alert, R., Blanch-Mercader, C. & Casademunt, J. Active fingering instability in tissue spreading. *Phys. Rev. Lett.* 122, 088104 (2019).
- Blanch-Mercader, C. et al. Effective viscosity and dynamics of spreading epithelia: a solvable model. Soft Matter 13, 1235–1243 (2017).
- Delanoë-Ayari, H., Bouchonville, N., Courçon, M. & Nicolas, A. Linear correlation between active and resistive stresses provides information on force generation and stress transmission in adherent cells. *Phys. Rev. Lett.* 129, 098101 (2022).
- 55. Brückner, D. B. et al. Stochastic nonlinear dynamics of confined cell migration in two-state systems. *Nat. Phys.* **15**, 595–601 (2019).
- Chan, C. E. & Odde, D. J. Traction dynamics of filopodia on compliant substrates. Science 322, 1687–1691 (2008).
- 57. Bangasser, B. L. et al. Shifting the optimal stiffness for cell migration. *Nat. Commun.* **8**, 15313 (2017).
- Bergert, M. et al. Force transmission during adhesion-independent migration. *Nat. Cell Biol.* 17, 524–529 (2015).
- Sakamoto, R., Izri, Z., Shimamoto, Y., Miyazaki, M. & Maeda, Y. T. Geometric trade-off between contractile force and viscous drag determines the actomyosin-based motility of a cell-sized droplet. *Proc. Natl Acad. Sci. USA* 119, e2121147119 (2022).

- Godeau, A. L. et al. 3D single cell migration driven by temporal correlation between oscillating force dipoles. eLife 11, e71032 (2022).
- 61. Carlsson, A. E. Mechanisms of cell propulsion by active stresses. *New J. Phys.* **13**, 073009 (2011).
- 62. Amiri, B., Heyn, J. C. J., Schreiber, C., Rädler, J. O. & Falcke, M. On multistability and constitutive relations of cell motion on fibronectin lanes. *Biophys. J.* **122**, 753–766 (2023).
- 63. Basan, M., Elgeti, J., Hannezo, E., Rappel, W.-J. & Levine, H. Alignment of cellular motility forces with tissue flow as a mechanism for efficient wound healing. *Proc. Natl Acad. Sci. USA* **110**, 2452–2459 (2013).
- 64. Ron, J. E. et al. Polarization and motility of one-dimensional multi-cellular trains. *Biophys. J.* **122**, 4598–4613 (2023).
- Camley, B. A. Collective gradient sensing and chemotaxis: modeling and recent developments. J. Phys. Condens. Matter 30, 223001 (2018).
- 66. Ruppel, A. et al. Force propagation between epithelial cells depends on active coupling and mechano-structural polarization. *eLife* **12**, e83588 (2023).
- 67. George, M., Bullo, F. & Campàs, O. Connecting individual to collective cell migration. Sci. Rep. **7**, 9720 (2017).
- Zimmermann, J., Camley, B. A., Rappel, W.-J. & Levine, H. Contact inhibition of locomotion determines cell-cell and cell-substrate forces in tissues. *Proc. Natl Acad. Sci. USA* 113, 2660–2665 (2016).
- 69. Boutillon, A. et al. Guidance by followers ensures long-range coordination of cell migration through  $\alpha$ -catenin mechanoperception. *Dev. Cell* **57**, 1529–1544.e5 (2022).
- Campanale, J. P. & Montell, D. J. Who's really in charge: diverse follower cell behaviors in collective cell migration. *Curr. Opin. Cell Biol.* 81, 102160 (2023).
- Alert, R. & Casademunt, J. Role of substrate stiffness in tissue spreading: wetting transition and tissue durotaxis. *Langmuir* 35, 7571–7577 (2019).

**Publisher's note** Springer Nature remains neutral with regard to jurisdictional claims in published maps and institutional affiliations.

Springer Nature or its licensor (e.g. a society or other partner) holds exclusive rights to this article under a publishing agreement with the author(s) or other rightsholder(s); author self-archiving of the accepted manuscript version of this article is solely governed by the terms of such publishing agreement and applicable law.

© The Author(s), under exclusive licence to Springer Nature Limited 2024

#### Methods

#### Cloning

The TIAM-CRY2-mCherry plasmid was constructed as detailed previously for lentiviral vectors<sup>37</sup>. The CIBN-GFP-CAAX plasmid was a gift from C. Tucker<sup>40</sup>.

#### Cell culture

MDCK strain II cells were cultured in the minimum essential medium with Earle's salts and L-glutamine (Gibco) supplemented with 10% v/v foetal bovine serum (Gibco), 100 U ml $^{-1}$  penicillin and 100  $\mu g$  ml $^{-1}$  streptomycin. Cells were maintained at 37 °C in a humidified atmosphere with 5% CO $_2$ . OptoMDCK-Rac1 fluorescent stable cell lines were obtained by the lentiviral transduction of CIBN-GFP-CAAX and TIAM-CRY2-mCherry and two rounds of flow-cytometry-based sorting.

#### Polyacrylamide gels

We prepared polyacrylamide gels with a stiffness of 18 kPa according to a previously established protocol and functionalized them with Sulpho-SANPAH (Thermo Fisher Scientific)72. For the gels, we prepared a solution of 0.16% bis-acrylamide and 7.50% acrylamide, 0.01% v/v 200-nm-diameter dark-red-fluorescent carboxylate-modified beads (FluoSpheres, Thermo Fisher Scientific), 0.50% v/v ammonium persulfate (Sigma-Aldrich) and 0.05% tetramethylethylenediamine (Sigma-Aldrich), in phosphate-buffered saline (PBS). We placed a 22 µl drop of unpolymerized gel on a glass-bottom MatTek 35 mm dish and immediately covered it with an 18 mm circular coverslip. The gels were then allowed to polymerize at room temperature for 1 h and then covered with PBS before removing the circular coverslip. Functionalization of the gel surface was achieved by incubation with a solution of 2 mg ml<sup>-1</sup> Sulpho-SANPAH under ultraviolet light for 7 min (wavelength of 365 nm at a distance of 5 cm). Then, two washes of PBS were performed for 2.5 min under mild agitation to remove excess Sulpho-SANPAH. The gels were then immediately used for microcontact printing of the fibronectin lines.

#### Microcontact printing

Stamps for microcontact printing of 20 µm lines were fabricated from SU8-50 masters that had been raised using conventional photolithography. For the 50 µm lines, the masters were produced by polymerizing a thin layer (20 µm) of photopolymerizing resin (NOA61, Norland) using an ultraviolet photopatterning device (PRIMO, Alvéole) coupled to an inverted microscope (Ti ECLIPSE, Nikon). In both cases, the masters contained tens of identical parallel line patterns (~10 mm × 5 mm). Within each pattern, the lines were spaced 80 µm from each other. Uncured polydimethylsiloxane (SYLGARD, Dow Corning) was poured on the masters and cured overnight at 65 °C. Solid polydimethylsiloxane stamps were then cut out and peeled off from the master, and their patterned surfaces were treated with a 15 s discharge from a handheld corona surface treater (APS-CD-20AC, Aurora Pro Scientific). Immediately following this, they were covered with a 100 µl drop of a solution of 20 µg ml<sup>-1</sup> fibronectin (fibronectin from human plasma, Sigma-Aldrich) and 15 μg ml<sup>-1</sup> fibrinogen-Alexa 488 conjugate (F13191, Thermo Fisher) and incubated at room temperature for 1 h. After this, the excess incubating solution was removed, and stamps were dried with a nitrogen gun. A polyacrylamide gel was thoroughly dried with a nitrogen gun and the stamp was laid on top of it, with the patterned face in contact with the gel surface. Gel and stamp were left in contact for 1 h after which 1 ml PBS was added to the MatTek dish. After 1 h, the stamp was lifted, and the patterned gels were passivated by incubating overnight at 4 °C with a solution of 0.1 mg ml<sup>-1</sup>PLL-g-PEG in PBS. Finally, the passivating solution was removed, and the gels were covered with a 300 µl drop of PBS and were immediately used for cell seeding.

#### **Cell seeding**

OptoMDCK-Rac1 cells were detached from their culture flask using trypsin and resuspended in culture medium. A 300 µl drop containing

 $2 \times 10^4$  cells was placed on a micropatterned gel that had been sterilized under ultraviolet light in a cell culture hood for 15 min. Cells were allowed to adhere for 1 h before unattached cells were removed by a gentle wash with warm cell culture media. The samples were then left to incubate for 12 h in 2 ml cell media containing 2 mM thymidine (T92502431G, Sigma) at 37 °C in a humidified atmosphere with 5% CO<sub>2</sub>.

#### Photoactivation experiments and fluorescence imaging

Experiments were carried out on a Zeiss LSM880 confocal microscope running the software Zeiss ZEN2.3 SP1FP3 (black, version 14.0.24.201), and using a Plan Apochromat ×20 0.8-numerical-aperture objective. Regions of the sample containing cell groups (trains or clusters) of interest were identified through the eyepieces using white light illumination with a long-pass red filter (cut-off at 630 nm). Only cell groups that were isolated from other cells on the same line were used for the experiments. The sample was rotated in the plane of the microscope stage so that the lines of the micropatterns appeared vertical in the images. Integrity of the micropatterned lines in each region was verified by acquiring a single image with a low-intensity 488 nm laser scan, visualizing the signal of the fibrinogen-Alexa 488 conjugate present in the protein coating. Regions with discontinuous or broken patterns were not used for the experiments. After this step, 45 min were allowed to pass to facilitate the unbinding of CRY2/CIBN and for any induced activation of Rac1 to return to the basal levels<sup>39</sup>. Following this, the imaging was started. Three channels were acquired: 561 nm to excite mCherry, 633 nm to excite the fluorescent microspheres and  $633\,nm\,transmitted\,light\,to\,obtain\,a\,bright\text{-}field\,image.\,Scanning\,was$ performed with a pixel size of 0.17  $\mu$ m and a pixel dwell time of 0.35  $\mu$ s. Up to four fields of view were acquired, with imaging occurring every 3 min in a multiposition time lapse. At each position, the fluorescence autofocus algorithm of ZEN was run using the microsphere fluorescence as the reference. Initially, a baseline phase of 2 h with no photoactivation was acquired. Following this, a subgroup of cell groups was selected to be photoactivated and a rectangular illumination region was drawn on the free edge of one of their edges using the ROI tool of ZEN. Imaging was then resumed as before, and during every subsequent imaging acquisition, the photoactivation regions were scanned with the 488 nm laser and the same pixel dwell time as before. Imaging and photoactivation continued for 4-5 h with a frequency of 3 min. After every five image acquisitions (that is, every 15 min), the positions of the photoactivating regions were manually adjusted according to the movement of the targeted cells. This was done to keep the region of induced lamellipodia at the same relative position within the cell group. This operation required less than 2 min. At the end of each experiment, cells were detached from the gel using Versene 1X (Life Technologies) and a reference image of the fluorescent beads was acquired for the TFM calculations<sup>42</sup>. Cell groups that merged or touched other cells and cell groups containing cells that divided during the experiment were not considered for analysis.

#### **Image analysis**

In the non-photoactivated cases, we calculated each cell train's average centre-of-mass velocity  $\langle V \rangle_t$  over the duration of the full experiment, whereas in the photoactivated cases, we computed  $\langle V \rangle_t$  from 1 h after photoactivation until the end of the experiment, to exclude any transient behaviour.

For all the time points, mCherry fluorescence images were semi-automatically segmented using a MATLAB (R2017a) script and ImageJ/FIJI (2.3.0/1.53f51). The first segmentation was obtained based on the triangle thresholding algorithm, and then any mistakes were manually corrected. The binary masks thus obtained were used to measure the cell group dynamics (edge trajectories and centre-of-mass trajectory). In the photoactivated cases, the images were reoriented (if necessary) so that the photoactivation region of interest was at a positive y distance from the centre of the cell group. Edge trajectories

were smoothed by adjacent averaging with a span of five points. Lamellipodium growth was calculated by first dividing the train segmentation into two by bisecting its major axis. The average area (A) of the top half (that is, the half subject to photoactivation) was calculated in the hour before and following photoactivation  $(A^*)$ . Lamellipodium growth was defined as the difference between these two areas:  $\Delta A = A^* - A$ .

#### Quantifying directed motion

Motility of an edge was characterized using the set of its instantaneous velocities. For each trajectory, a two-sided Wilcoxon signed-rank test was applied to assess if the set of instantaneous velocities was significantly different from a set with a null median. If it was not, the edge was considered to be not significantly motile in any direction. In the case of non-photoactivated trains, this approach was applied to trajectories lasting for the whole duration of the experiment, whereas in the other cases, it was separately applied to the trajectories before and during photoactivation, but to rule out any transient effect caused by photoactivation, we left out the first hour after its application. For a cell train, directed and antidirected motion were defined as the cases when the aforementioned analysis yielded that the median velocities of both edges were significantly non-zero and of the same sign.

#### TFM and traction force data analysis

All the traction computations and the following analyses of traction forces were carried out with MATLAB scripts. Fourier transform traction microscopy was used to measure the traction forces<sup>29,44,73</sup>. The displacement fields of the fluorescence microspheres were obtained using a home-made particle imaging velocimetry algorithm using square interrogation windows with a side of 40 pixels and an overlap of 0.8. The segmented binary masks of the cell trains obtained from the mCherry fluorescence were used to segment the tractions for each train at each time point. The axial profiles of the tractions were calculated by averaging the y component of the tractions  $T_{yy}$  across the width of the segmented cell trains, at every time point, yielding  $\langle T_{\nu} \rangle_{x}$ . The axial lengths of these profiles were normalized to unit length for each time point and the tractions were averaged together in groups according to the train's behaviour (directed/antidirected motion, or not). In the photoactivated cases, only the time points starting 1 h after photoactivation were considered. The same averaging procedure was applied to obtain the axial tension profiles from  $\sigma_{v}(y,t) = \int_{0}^{y} [T_{v}(y,t)/h] dy$ , where h is the height of the cell and is approximated to be 10 µm. The normalized second moment of the traction field was calculated as  $Q(t) = (\int T_y y^2 dy) / (\int |T_y| y^2 dy)$ , where y is the spatial coordinate relative to the centre of mass, and was then averaged over time, adapting the durations to the photoactivated and non-photoactivated cases, as explained above.

#### Calculation of cell-cell tension

Calculations were performed under the assumption that the cell train behaves as a 1D material. In that case, the Cauchy stress tensor is reduced to a scalar  $\sigma$ , which we refer to as tension. The equation of mechanical equilibrium in one dimension reads  $\frac{\partial \sigma}{\partial y} = -T_y$ ; hence, internal tension can be obtained by the direct integration of the traction field<sup>29,74,75</sup>.

#### Kymographs

Kymographs of tractions were obtained by averaging across the x axis the 2D traction maps of  $T_y(y,t)$ , at each individual time point. The values of  $\langle T_y \rangle_x$  were plotted in a colour-coded figure in the order and spacing given by the experiment's acquisition times.

#### **Immunostainings**

OptoMDCK-Rac1 cells were photoactivated for 15 min, as explained above, and immediately fixed with 4% paraformaldehyde during 15 min at room temperature. Then, cells were washed three times with PBS.

The immunostainings were performed at room temperature using Tris-buffered saline containing 1.6% (v/v) fish gelatine (G7765, Merck) as the basal buffer. First, permeabilization was carried out by treating the samples with 0.1% Triton X-100 (T8787, Sigma-Aldrich) during 45 min. After that, samples were incubated for 90 min with the primary antibody (rabbit anti-phospho-paxillin; 69363s, Cell Signaling) diluted 1:100. After three 3-min washes, samples were incubated for 90 min with the secondary antibody (Alexa Fluor 647 goat anti-rabbit; A-21245, Thermo Fisher) diluted 1:200. Finally, they were washed four times for 3 min with PBS and mounted in MOWIOL reagent (81381, Merck). The image acquisition was done on a Zeiss LSM880 confocal microscope running the software Zeiss ZEN2.3 SP1FP3 (black, version 14.0.24.201), and using a Plan Apochromat ×20 0.8-numerical-aperture objective. The photoactivated cells were identified for imaging by using the microscope software to return to the previously stored positions and visually confirming that the same field of view had been reached.

#### Fits of theoretical model to experimental results

Equation (1) was fitted to the experimental data displayed in Fig. 3d (top row).  $T_a$  is given by equation (2) in terms of  $\zeta_+$ ,  $\zeta_-$ ,  $\ell_+$ ,  $\ell_-$  and L. As the velocity v varies weakly in space, it was replaced in equation (1) with the average velocity V for simplicity. Thus, the fits yield values for the parameters  $\zeta_+$ ,  $\zeta_-$ ,  $\ell_+$ ,  $\ell_-$  and  $\xi V$ . The fit was performed using the MATLAB function fitnlm. Confidence intervals for the parameters are the 95% confidence bounds, as given by the MATLAB function confint.

#### Simulating the relationship between Q and V

To generate the simulated plot of Q against V (Fig. 4s), we fitted the model equations to experimental traction profiles  $\langle T_{\nu} \rangle_{r}$  as described above, but for each coherently moving cell train individually. These fits yielded a set of optimal values for the parameters  $(\zeta_+, \zeta_-, \ell_+, \ell_-)$  and  $\xi V$ for each of the 60 moving trains. We used the measured centre-of-mass velocity V of each train to obtain values of  $\xi$  and calculated its average  $\langle \xi \rangle$  for each train length  $N_c$ . We did not consider the fits that had diverging values of  $\ell_+$  and  $\ell_-$ , leaving us with 43 out of the 60 fits. From the fit results, we built the empirical distributions of the parameter values for  $\zeta_+, \zeta_-, \ell_+$  and  $\ell_-$  for each train length. We approximated these empirical distributions by Gaussian distributions with the mean and standard deviation obtained from the fit results. To generate the Q(V) plot, we sampled the Gaussian distributions and obtained 15 sets of parameters values  $\zeta_1, \zeta_2, \ell_1$  and  $\ell_2$  for each train length. Then, combining these 15 sets with the values of  $\langle \xi \rangle$  for each of the four train lengths  $N_c$ , we obtained 60 sets of parameter values with distributions similar to the empirical ones. For each of these 60 model realizations, we calculated the train velocity according to equation (3), and the quadrupole of the total traction force (see the 'TFM and traction force data analysis' section), resulting in the scatter plot shown in Fig. 5s.

#### Statistical tests, box plots and Sankey diagrams

All the statistical significance analyses were performed using a two-sided Wilcoxon rank-sum test, as implemented by the MATLAB functions ranksum and signrank. Box plots in all the figures show the median value and the 25th and 75th percentiles of the data. The whiskers have a set length of 1.5 times the interquartile range (difference between the 75th and 25th percentiles). Sankey diagrams were generated using the MATLAB function for Sankey flow charts<sup>76</sup>.

#### **Reporting summary**

Further information on research design is available in the Nature Portfolio Reporting Summary linked to this article.

#### Data availability

The full datasets that support the findings of this study are available from the corresponding authors on reasonable request. Source data are provided with this paper.

#### **Code availability**

Analysis procedures and codes are available via GitHub under a GPL-3.0 license at https://github.com/xt-prc-lab/Rossetti\_et\_al\_2024\_Nature\_Physics. All other codes are available from the corresponding authors on reasonable request.

#### References

- Serra-Picamal, X. et al. Mechanical waves during tissue expansion. Nat. Phys. 8, 628–634 (2012).
- Serra-Picamal, X., Conte, V., Sunyer, R., Muñoz, J. J. & Trepat, X. in Methods in Cell Biology Vol. 125 (Elsevier, 2015).
- 74. Tambe, D. T. et al. Collective cell guidance by cooperative intercellular forces. *Nat. Mater.* **10**, 469–475 (2011).
- Tambe, D. T. et al. Monolayer stress microscopy: limitations, artifacts, and accuracy of recovered intercellular stresses. PLoS ONE 8, e55172 (2013).
- Borau, C. Sankey flow chart. MATLAB Central File Exchange https://www.mathworks.com/matlabcentral/fileexchange/1015 16-sankey-flow-chart (2022).

#### **Acknowledgements**

We thank all the members of our groups for their discussions and support. We thank S. Usieto and M. Purciolas for technical assistance. We also thank C. Tucker (Department of Pharmacology, University of Colorado) and S. D. Beco (Institut Jacques Monod) for sharing the plasmids used in this work. We thank P. Silberzan (Institut Curie) for sharing the experimental data with us. Finally, we thank I. Andreu, M. Matejčić and A. Beedle for discussions and feedback on the manuscript. This paper was funded by the Generalitat de Catalunya (AGAUR SGR-2017-01602 to X.T.; the CERCA Programme and 'ICREA Academia' awards to P.R.-C.); the Spanish Ministry for Science and Innovation MICCINN/FEDER (PID2021-128635NB-I00, MCIN/AEI/10.13039/501100011033 and 'ERDF-EU A way of making Europe' to X.T.; PID2019-110298GB-I00 to P.R.-C.); European Research Council (101097753 to P.R.-C. and Adv-883739 to X.T.); Fundació la Marató

de TV3 (project 201903-30-31-32 to X.T.); European Commission (H2020-FETPROACT-01-2016-731957 to P.R.-C. and X.T.); the European Union's Horizon 2020 research and innovation programme (under the Marie Skłodowska-Curie grant agreement ID 796883 to L.R.); La Caixa Foundation (LCF/PR/HR20/52400004 to P.R.-C. and X.T.); IBEC is recipient of a Severo Ochoa Award of Excellence from MINECO.

#### **Author contributions**

L.R., L.V. and X.T. conceived the project. L.V. designed and performed the preliminary experiments. L.R. and J.F.A. designed and performed the experiments. L.R. and S.G. analysed the data. J.F.A. and P.R.-C. contributed to the technical expertise, materials and discussion. R.A. developed the model. L.R., R.A. and X.T. wrote the manuscript. All authors revised the completed manuscript.

#### **Competing interests**

The authors declare no competing interests.

#### **Additional information**

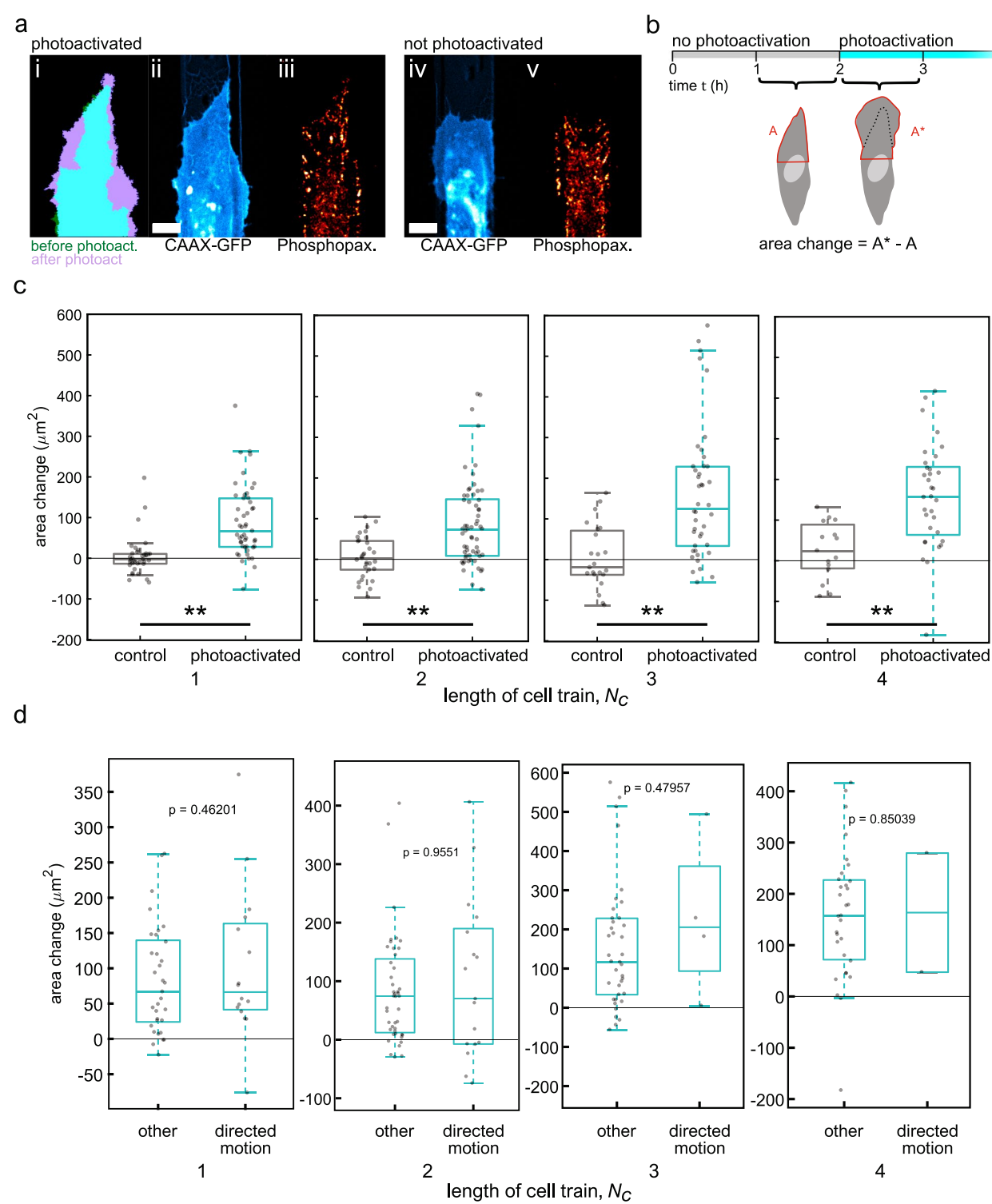
**Extended data** is available for this paper at https://doi.org/10.1038/s41567-024-02600-2.

**Supplementary information** The online version contains supplementary material available at https://doi.org/10.1038/s41567-024-02600-2.

**Correspondence and requests for materials** should be addressed to Leone Rossetti, Ricard Alert or Xavier Trepat.

**Peer review information** *Nature Physics* thanks Yusuke Maeda, and the other, anonymous, reviewer(s) for their contribution to the peer review of this work.

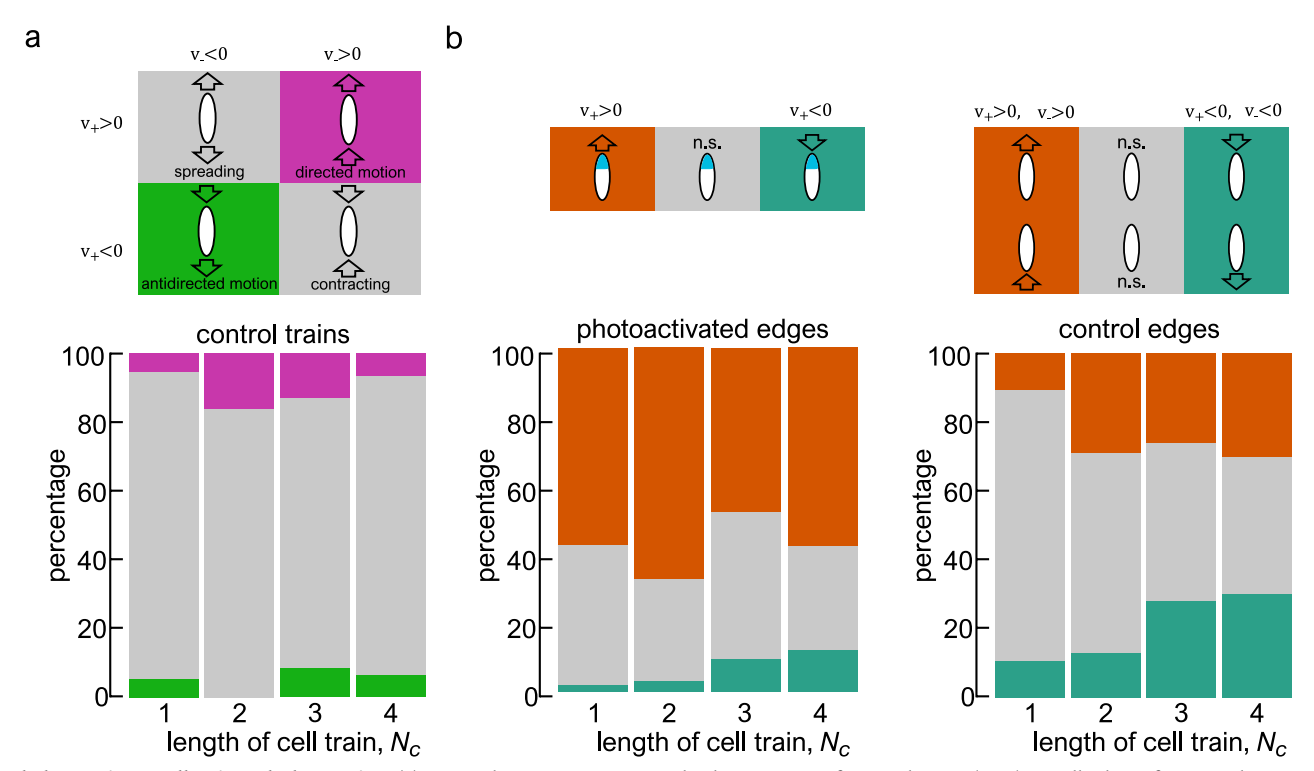
**Reprints and permissions information** is available at www.nature.com/reprints.



#### Extended Data Fig. 1 | Photoactivation induces lamellipodium growth.

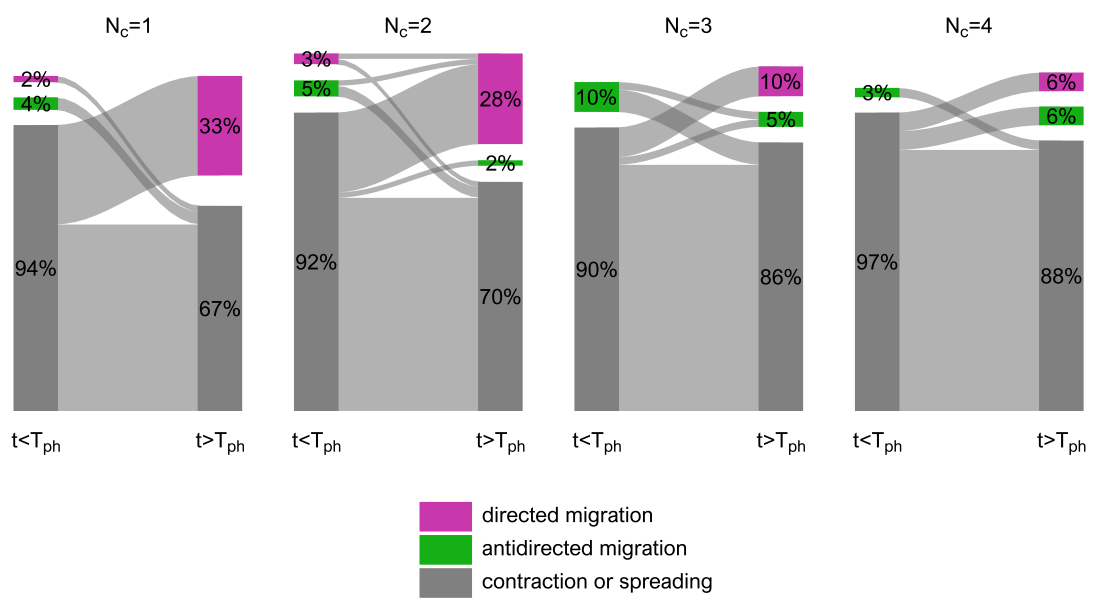
(a) (i) Segmentation of a lamellipodium before (green) and after photoactivation (lilac, cyan is the overlap), (ii) membrane fluorescence of lamellipodium after photoactivation, (iii) focal adhesions after photoactivation, (iv) a naturally occurring lamellipodium, (v) focal adhesions in the naturally occurring lamellipodium (scale bar  $10~\mu m$ ). Similar results were obtained in n=10~cell trains from 3 independent experiments. (b) Scheme of how lamellipodium area is calculated. The area of the top half of the cell is averaged during 1~h prior to (A) and following (A\*) photoactivation (these same time intervals are considered also for control cells). The change of lamellipodium size is calculated as the difference between A\* and A. (c) Lamellipodium area for trains of different lengths,

comparing control cases and photoactivated trains. Photoactivation induces lamellipodium growth in nearly all cases. Statistical significance quantified by a two-sided Wilcoxon rank sum test, \*\* indicates p<0.01. Box plots showing first quartile, median and third quartile. Range includes all data points. Whiskers extend to first adjacent value within 1.5 x inter-quartile range. Full p-values in Supplementary Table 1. (d) Lamellipodium growth of photoactivated trains undergoing directed motion compared with other trains. Lamellipodium growth is not significantly different between these two subpopulations. Statistical significance quantified by a two-sided Wilcoxon rank sum test. Box plots showing first quartile, median and third quartile. Range includes all data points. Whiskers extend to first adjacent value within 1.5 x inter-quartile range.



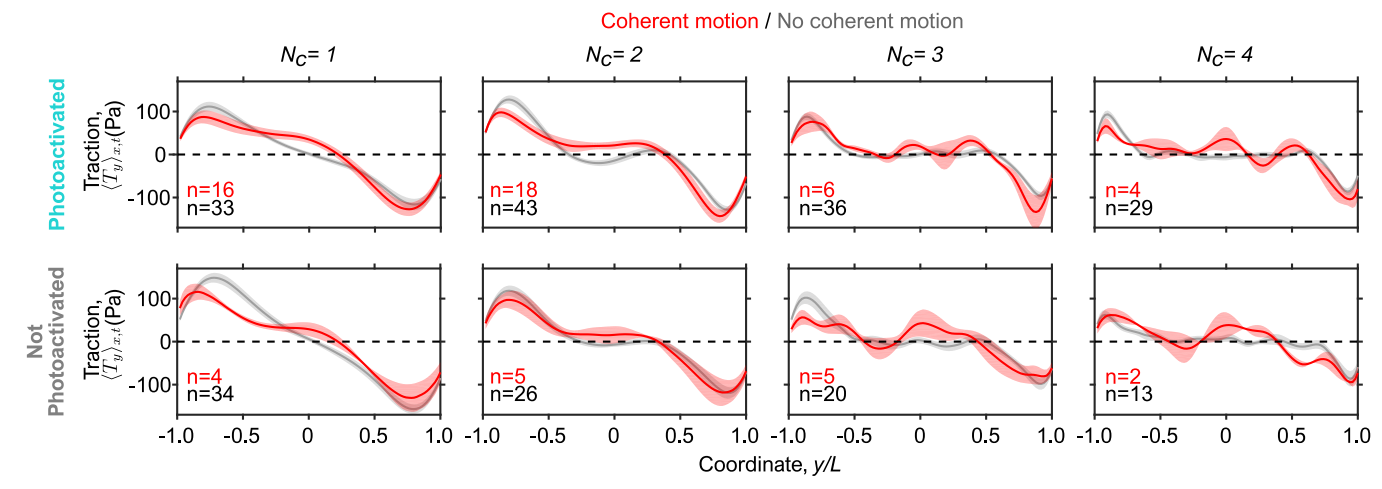
**Extended Data Fig. 2** | **Cell train and edge motion.** (a) Directed migration in control trains. In absence of photoactivation there is an equal probability for upwards (directed) or downwards (antidirected) migration. (b) Effect of photoactivation on edge motion, compared with control cases. The bars show the percentage of photoactivated edges that have significant velocities in the direction of photoactivation (magenta), in the opposing direction (green), or

that have non-significant velocities (grey). For all values of  $N_c$  more than 50% of the cell trains have edge velocities biased in the direction of the induced lamellipodium. In the control case, both directions are equally probable. For increasing values of  $N_c$  the photoactivated edges total sample sizes are n=49, n=61, n=42, n=33, respectively, and for the control edges total sample sizes are n=38, n=31, n=23, n=15.



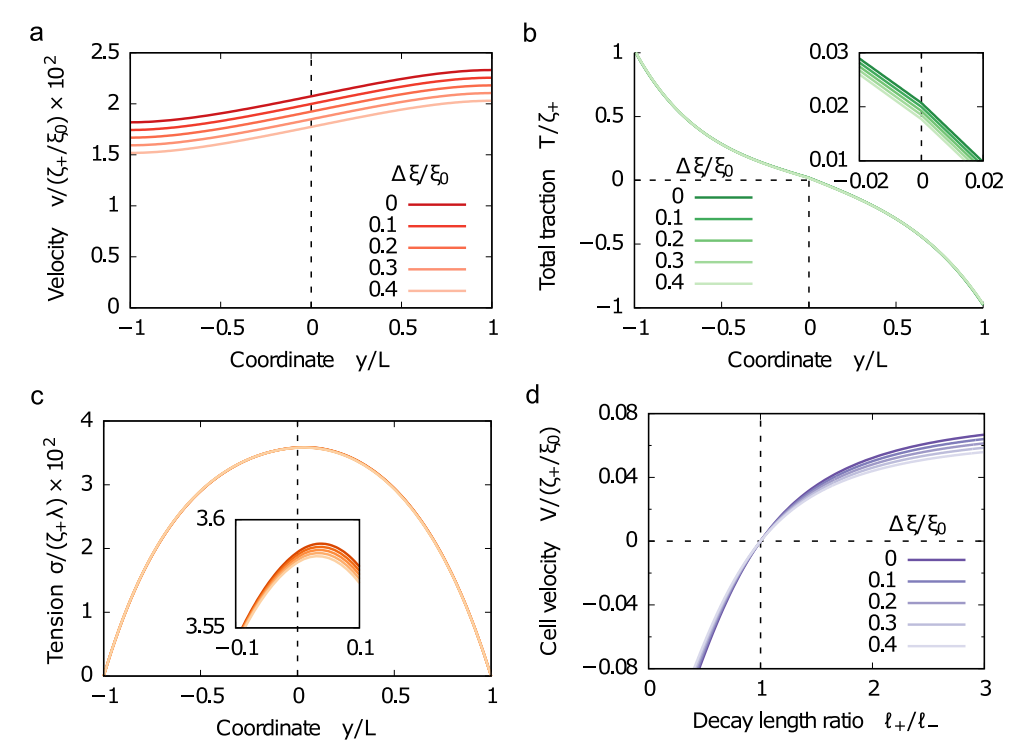
Extended Data Fig. 3 | Photoactivated cell trains that undergo directed migration are not undergoing directed migration prior to photoactivation. Motion of cell trains of different lengths before and during photoactivation. For each value of  $N_c$  the column on the left shows the type of migration of the trains that will be photoactivated, while the column on the right shows the type of

migration of the same trains during photoactivation (same data as Fig. 2e). The stripes connecting the columns show how cell trains changed their migration type due to photoactivation.  $T_{ph}$  stands for the time at which photoactivation starts and t is time.



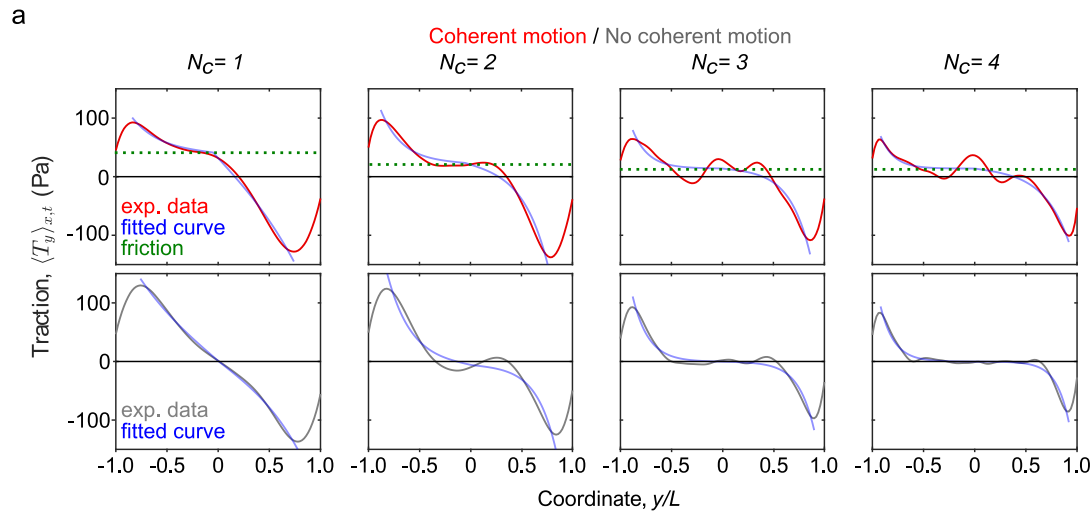
**Extended Data Fig. 4** | **Effect of photoactivation on traction forces.** Average profiles of the longitudinal component of the traction for cell trains undergoing coherent motion (red) and for other trains (grey). The top row shows only

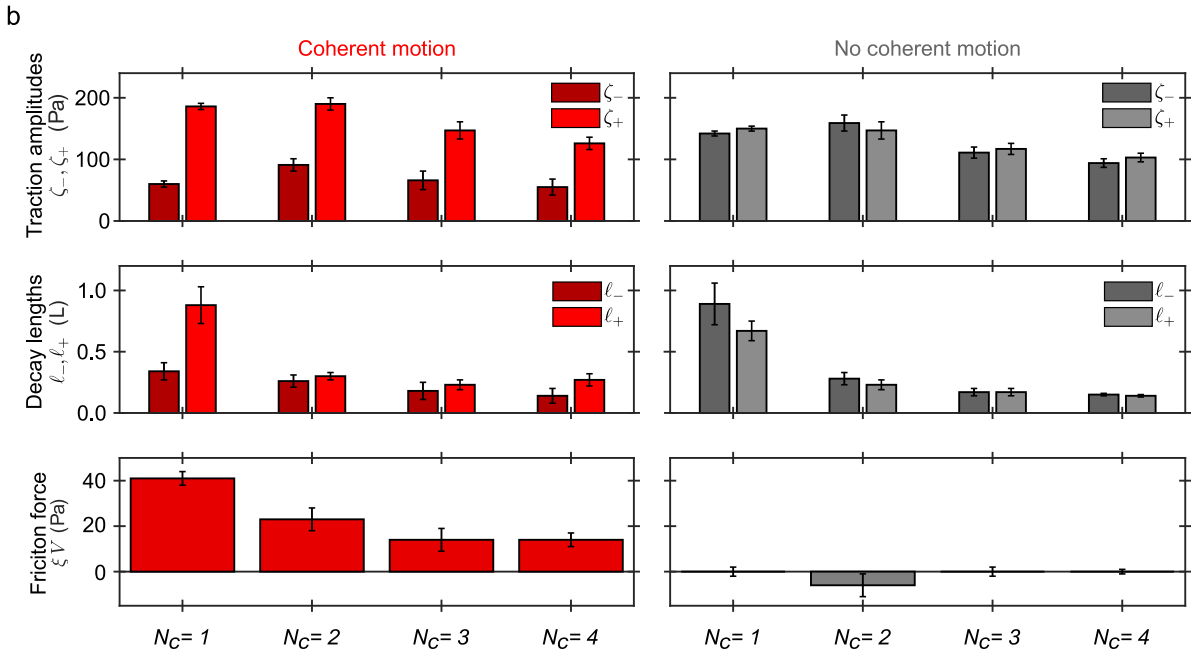
photoactivated trains, the bottom row non-photoactivated trains. Shaded regions along the curves show the standard error of the mean. Averages are over different cell trains; number of cell trains n is indicated on the plot.



**Extended Data Fig. 5** | **Role of non-uniform friction on train motion.** (a-c) Predicted profiles of velocity (a), total traction (b), and tension (c) for different values of the relative strength of friction non-uniformity,  $\Delta \xi/\xi_0$ , varied from 0% to 40%. Insets help to visualize the small effect of friction non-uniformity. The theory with non-uniform friction is explained in Section D of the

Supplementary Note. (d) Centre-of-mass velocity as a function of the decaylength asymmetry of the active tractions, as in Fig. 50, shown for different values of the relative friction non-uniformity. The effects of friction non-uniformity are small in all cases. In all panels, we chose  $\zeta_+=\zeta_-$ ,  $\ell_-=0.4$  L, and  $\lambda=10L$ . In panels a-c, we chose  $\ell_+/\ell_-=1.25$ .





**Extended Data Fig. 6** | **Fits of the predicted traction profiles to the experimental data. (a)** Model (blue curves) and experimental (red and grey curves) average longitudinal tractions for cell trains undergoing coherent motion (top row, red curves) and for other trains (bottom row, grey curves).

In the top row, dashed green lines show the level of friction force, as also reported in the bottom left plot of panel (b). (b) Parameter values of the model (equation (1)) obtained from the fits. Error bars are confidence intervals derived from the fits (see Methods).

# nature portfolio

Corresponding author(s):	Leone Rossetti, Ricard Alert, Xavier Trepat
Last updated by author(s):	Apr 29, 2024

## **Reporting Summary**

Nature Portfolio wishes to improve the reproducibility of the work that we publish. This form provides structure for consistency and transparency in reporting. For further information on Nature Portfolio policies, see our <u>Editorial Policies</u> and the <u>Editorial Policy Checklist</u>.

For all statistical analyses, confirm that the following items are present in the figure legend, table legend, main text, or Methods section.

_					
ζ.	ta:	t١	ct	т	2

n/a	Confirmed		
	The exact	sample size $(n)$ for each experimental group/condition, given as a discrete number and unit of measurement	
	X A stateme	ent on whether measurements were taken from distinct samples or whether the same sample was measured repeatedly	
	The statis	tical test(s) used AND whether they are one- or two-sided on tests should be described solely by name; describe more complex techniques in the Methods section.	
	A descript	ion of all covariates tested	
$\boxtimes$	A descript	ion of any assumptions or corrections, such as tests of normality and adjustment for multiple comparisons	
	A full description of the statistical parameters including central tendency (e.g. means) or other basic estimates (e.g. regression coefficient) AND variation (e.g. standard deviation) or associated estimates of uncertainty (e.g. confidence intervals)		
	For null hypothesis testing, the test statistic (e.g. <i>F</i> , <i>t</i> , <i>r</i> ) with confidence intervals, effect sizes, degrees of freedom and <i>P</i> value noted Give <i>P</i> values as exact values whenever suitable.		
$\boxtimes$	For Bayesian analysis, information on the choice of priors and Markov chain Monte Carlo settings		
$\boxtimes$	For hierarchical and complex designs, identification of the appropriate level for tests and full reporting of outcomes		
$\boxtimes$	Estimates of effect sizes (e.g. Cohen's <i>d</i> , Pearson's <i>r</i> ), indicating how they were calculated		
Our web collection on <u>statistics for biologists</u> contains articles on many of the points above.			
Sof	ftware an	d code	
Polic	cy information	about <u>availability of computer code</u>	
Da	ta collection	ZEN2.3 SP1 FP3 (black, version 14.0.24.201)	
Da	ta analysis	MATLAB version R2017a, MathWorks Inc., Natick, Massachusetts, 2017. Custom made codes can be made available upon reasonable request to the corresponding authors. ImageJ/Fiji (2.3.0/1.53f51) was used for image pre-processing and segmentation.	
	For manuscripts utilizing custom algorithms or software that are central to the research but not yet described in published literature, software must be made available to editors and reviewers. We strongly encourage code deposition in a community repository (e.g. GitHub). See the Nature Portfolio guidelines for submitting code & software for further information.		

Policy information about availability of data

Data

All manuscripts must include a data availability statement. This statement should provide the following information, where applicable:

- Accession codes, unique identifiers, or web links for publicly available datasets
- A description of any restrictions on data availability
- For clinical datasets or third party data, please ensure that the statement adheres to our policy

The data that support the findings of this study are available from the corresponding authors on reasonable request.

## Field-specific reporting

riela specific reporting		
Please select the one below that is the best fit for your research. If you are not sure, read the appropriate sections before making your selection.		
Life sciences Behavioural & social sciences Ecological, evolutionary & environmental sciences		
For a reference copy of the document with all sections, see <u>nature.com/documents/nr-reporting-summary-flat.pdf</u>		
Life scier	nces study design	
All studies must dis	sclose on these points even when the disclosure is negative.	
Sample size	No statistical test was used to determine sample size. Sample size was determined empirically according to previous knowledge of the variation in similar experimental setups. For cell trains and clusters, experiments were performed until all train types and clusters were represented by at least n=40 individual cases, which is sufficient to detect meaningful differences based on historical record with similar experiments.	
Data exclusions	Cell trains that included a dividing cell, and cell trains that touched other cell trains during the experiment were not considered for analysis.	
Replication	Experiments were replicated 59 times to obtain a data-set of 292 independent cell trains and 8 times to obtain 43 cell clusters. Experiments were performed on different days and with different cell batches, obtaining the same results.	
Randomization	No randomization method for the selection of cell trains or clusters was applied. Trains and clusters were selected solely on the basis of 1) if	
Natiouthization	they occurred on intact fibronectin patterns, 2) whether they were far from other cells, 3) if 1 and 2 were met, then regions containing more than one viable cell train or cluster were favoured. This selection process could not introduce any bias as the selection criteria were not related to any properties of the cells.	

## Behavioural & social sciences study design

All studies must disclose on these points even when the disclosure is negative.

both produced and analysed the data.

Study description

Blinding

Briefly describe the study type including whether data are quantitative, qualitative, or mixed-methods (e.g. qualitative cross-sectional, quantitative experimental, mixed-methods case study).

Researchers were not blinded to group allocation during data collection and/or analysis. Blinding was not possible as the same researchers

Research sample

State the research sample (e.g. Harvard university undergraduates, villagers in rural India) and provide relevant demographic information (e.g. age, sex) and indicate whether the sample is representative. Provide a rationale for the study sample chosen. For studies involving existing datasets, please describe the dataset and source.

Sampling strategy

Describe the sampling procedure (e.g. random, snowball, stratified, convenience). Describe the statistical methods that were used to predetermine sample size OR if no sample-size calculation was performed, describe how sample sizes were chosen and provide a rationale for why these sample sizes are sufficient. For qualitative data, please indicate whether data saturation was considered, and what criteria were used to decide that no further sampling was needed.

Data collection

Provide details about the data collection procedure, including the instruments or devices used to record the data (e.g. pen and paper, computer, eye tracker, video or audio equipment) whether anyone was present besides the participant(s) and the researcher, and whether the researcher was blind to experimental condition and/or the study hypothesis during data collection.

Timing

Indicate the start and stop dates of data collection. If there is a gap between collection periods, state the dates for each sample cohort.

Data exclusions

If no data were excluded from the analyses, state so OR if data were excluded, provide the exact number of exclusions and the rationale behind them, indicating whether exclusion criteria were pre-established.

Non-participation

 $State\ how\ many\ participants\ dropped\ out/declined\ participation\ and\ the\ reason(s)\ given\ OR\ provide\ response\ rate\ OR\ state\ that\ no\ participants\ dropped\ out/declined\ participation.$ 

Randomization

If participants were not allocated into experimental groups, state so OR describe how participants were allocated to groups, and if allocation was not random, describe how covariates were controlled.

## Ecological, evolutionary & environmental sciences study design

ıll studies must disclose or	n these points even when the disclosure is negative.	
Study description	Briefly describe the study. For quantitative data include treatment factors and interactions, design structure (e.g. factorial, nested, hierarchical), nature and number of experimental units and replicates.	
Research sample	Describe the research sample (e.g. a group of tagged Passer domesticus, all Stenocereus thurberi within Organ Pipe Cactus National Monument), and provide a rationale for the sample choice. When relevant, describe the organism taxa, source, sex, age range and any manipulations. State what population the sample is meant to represent when applicable. For studies involving existing datasets, describe the data and its source.	
Sampling strategy	Note the sampling procedure. Describe the statistical methods that were used to predetermine sample size OR if no sample-size calculation was performed, describe how sample sizes were chosen and provide a rationale for why these sample sizes are sufficient.	
Data collection	Describe the data collection procedure, including who recorded the data and how.	
Timing and spatial scale	Indicate the start and stop dates of data collection, noting the frequency and periodicity of sampling and providing a rationale for these choices. If there is a gap between collection periods, state the dates for each sample cohort. Specify the spatial scale from which the data are taken	
Data exclusions	If no data were excluded from the analyses, state so OR if data were excluded, describe the exclusions and the rationale behind them, indicating whether exclusion criteria were pre-established.	
Reproducibility	Describe the measures taken to verify the reproducibility of experimental findings. For each experiment, note whether any attempts to repeat the experiment failed OR state that all attempts to repeat the experiment were successful.	
Randomization	Describe how samples/organisms/participants were allocated into groups. If allocation was not random, describe how covariates were controlled. If this is not relevant to your study, explain why.	
Blinding	Describe the extent of blinding used during data acquisition and analysis. If blinding was not possible, describe why OR explain why blinding was not relevant to your study.	
ield work, collec	tion and transport  Describe the study conditions for field work, providing relevant parameters (e.g. temperature, rainfall).	
Field conditions		
Location	State the location of the sampling or experiment, providing relevant parameters (e.g. latitude and longitude, elevation, water depth).	
Access & import/export	Describe the efforts you have made to access habitats and to collect and import/export your samples in a responsible manner and in compliance with local, national and international laws, noting any permits that were obtained (give the name of the issuing authority, the date of issue, and any identifying information).	
Disturbance	Describe any disturbance caused by the study and how it was minimized.	
e require information from a stem or method listed is rele	or specific materials, systems and methods authors about some types of materials, experimental systems and methods used in many studies. Here, indicate whether each material evant to your study. If you are not sure if a list item applies to your research, read the appropriate section before selecting a response.	
Vaterials & experime /a   Involved in the study	<del></del>	
/a   Involved in the study	n/a   Involved in the study   ChIP-seq	
Eukaryotic cell lines		
Palaeontology and a		
Animals and other of		
Human research pa		
Clinical data		
Dual use research o	f concern	

#### **Antibodies**

Antibodies used

The antibodies used were rabbit anti-phospho-paxillin (69363s, Cell Signaling) and Alexa Fluor-647 goat anti-rabbit (A-21245, ThermoFisher).

Validation

Both antibodies were used for immunofluorescence. The Phospho-Paxillin (Tyr118) (E9U9F) rabbit antibody (Cell Signaling #69363) has been tested by the manufacturer and by, at least, 19 previous publications (all of them can be found in the manufacturer webpage: https://www.cellsignal.com/product/productDetail.jsp?productId=69363). Figures of experiments that demonstrate specificity in western blot and immunofluorescence assays are depicted in the manufacturer webpage. The goat anti-rabbit IgG (H+L) highly cross-adsorbed secondary antibody with Alexa Fluor™ 647 (ThermoFisher #A-21245) was validated as displayed in the Antibody Registry, under the RRID number AB\_2535813 (https://www.antibodyregistry.org/AB\_2535813).

#### Eukaryotic cell lines

Policy information about cell lines

Cell line source(s)

The cell line used in this study (optoMDCK-Rac1) was derived from MDCK cells extensively used in our laboratory (see specifically doi: 10.1038/ncomms14396) and were originally provided by Guillaume Charras (UCL).

Authentication

None of the cell lines used were authenticated.

Mycoplasma contamination

All cell lines used in this work tested negative for Mycoplasma.

Commonly misidentified lines (See ICLAC register)

no commonly misidentified cell lines were used

#### Palaeontology and Archaeology

Specimen provenance

Provide provenance information for specimens and describe permits that were obtained for the work (including the name of the issuing authority, the date of issue, and any identifying information). Permits should encompass collection and, where applicable, export.

Specimen deposition

Indicate where the specimens have been deposited to permit free access by other researchers.

Dating methods

If new dates are provided, describe how they were obtained (e.g. collection, storage, sample pretreatment and measurement), where they were obtained (i.e. lab name), the calibration program and the protocol for quality assurance OR state that no new dates are provided.

Tick this box to confirm that the raw and calibrated dates are available in the paper or in Supplementary Information.

Ethics oversight

Identify the organization(s) that approved or provided guidance on the study protocol, OR state that no ethical approval or guidance was required and explain why not.

Note that full information on the approval of the study protocol must also be provided in the manuscript.

#### Animals and other organisms

Policy information about studies involving animals; ARRIVE guidelines recommended for reporting animal research

Laboratory animals

For laboratory animals, report species, strain, sex and age OR state that the study did not involve laboratory animals.

Wild animals

Provide details on animals observed in or captured in the field; report species, sex and age where possible. Describe how animals were caught and transported and what happened to captive animals after the study (if killed, explain why and describe method; if released, say where and when) OR state that the study did not involve wild animals.

Field-collected samples

For laboratory work with field-collected samples, describe all relevant parameters such as housing, maintenance, temperature, photoperiod and end-of-experiment protocol OR state that the study did not involve samples collected from the field.

Ethics oversight

Identify the organization(s) that approved or provided guidance on the study protocol, OR state that no ethical approval or guidance was required and explain why not.

Note that full information on the approval of the study protocol must also be provided in the manuscript.

## Human research participants

Policy information about studies involving human research participants

Population characteristics

Describe the covariate-relevant population characteristics of the human research participants (e.g. age, gender, genotypic information, past and current diagnosis and treatment categories). If you filled out the behavioural & social sciences study design questions and have nothing to add here, write "See above."

Recruitment	Describe how participants were recruited. Outline any potential self-selection bias or other biases that may be present and how these are likely to impact results.		
Ethics oversight	Identify the organization(s) that approved the study protocol.		
Note that full information on t	he approval of the study protocol must also be provided in the manuscript.		
Clinical data			
Policy information about <u>cl</u> All manuscripts should comply	inical studies with the ICMJE guidelines for publication of clinical research and a completed CONSORT checklist must be included with all submissions.		
Clinical trial registration	Provide the trial registration number from ClinicalTrials.gov or an equivalent agency.		
Study protocol	Note where the full trial protocol can be accessed OR if not available, explain why.		
Data collection	Describe the settings and locales of data collection, noting the time periods of recruitment and data collection.		
Outcomes	Describe how you pre-defined primary and secondary outcome measures and how you assessed these measures.		
Dual use research	o of concern		
'olicy information about <u>di</u>	ual use research of concern		
Hazards			
Could the accidental, delin the manuscript, pose a	iberate or reckless misuse of agents or technologies generated in the work, or the application of information presented a threat to:		
No   Yes			
Public health			
National security			
Crops and/or lives	:ock		
Ecosystems	Ecosystems		
Any other significa	nt area		
Experiments of conce	'n		
	y of these experiments of concern:		
No Yes			
Demonstrate how	to render a vaccine ineffective		
Confer resistance	to therapeutically useful antibiotics or antiviral agents		
Enhance the virulence of a pathogen or render a nonpathogen virulent			
Increase transmiss	Increase transmissibility of a pathogen		
Alter the host rang	Alter the host range of a pathogen		
Enable evasion of diagnostic/detection modalities			
Enable the weapon	Enable the weaponization of a biological agent or toxin		
Any other potentia	ally harmful combination of experiments and agents		
ChIP-seg			
<u> </u>			
Data deposition			
	v and final processed data have been deposited in a public database such as <u>GEO</u> .		
Confirm that you have	e deposited or provided access to graph files (e.g. BED files) for the called peaks.		

Data access links

May remain private before publication.

For "Initial submission" or "Revised version" documents, provide reviewer access links. For your "Final submission" document, provide a link to the deposited data.

Files in database submission

Provide a list of all files available in the database submission.

Genome browser session (e.g. <u>UCSC</u>)

Provide a link to an anonymized genome browser session for "Initial submission" and "Revised version" documents only, to enable peer review. Write "no longer applicable" for "Final submission" documents.

# Methodology Replicates Describe the experimental replicates, specifying number, type and replicate agreement. Sequencing depth Describe the sequencing depth for each experiment, providing the total number of reads, uniquely mapped reads, length of reads and whether they were paired- or single-end.

Antibodies

Describe the antibodies used for the ChIP-seq experiments; as applicable, provide supplier name, catalog number, clone name, and lot

Peak calling parameters | Specify the command line program and parameters used for read mapping and peak calling, including the ChIP, control and index files

Data quality

Describe the methods used to ensure data quality in full detail, including how many peaks are at FDR 5% and above 5-fold enrichment.

Software

Describe the software used to collect and analyze the ChIP-seq data. For custom code that has been deposited into a community repository, provide accession details.

#### Flow Cytometry

Plots

Instrument

Confirm that:		
The axis labels state the marker and fluorochrome used (e.g. CD4-FITC).		
The axis scales are clearly vis	ible. Include numbers along axes only for bottom left plot of group (a 'group' is an analysis of identical markers).	
All plots are contour plots wi	th outliers or pseudocolor plots.	
A numerical value for number of cells or percentage (with statistics) is provided.		
Methodology		
Sample preparation	Describe the sample preparation, detailing the biological source of the cells and any tissue processing steps used.	

Software

Describe the software used to collect and analyze the flow cytometry data. For custom code that has been deposited into a community repository, provide accession details.

Identify the instrument used for data collection, specifying make and model number.

Cell population abundance

Describe the abundance of the relevant cell populations within post-sort fractions, providing details on the purity of the samples and how it was determined.

Gating strategy

Describe the gating strategy used for all relevant experiments, specifying the preliminary FSC/SSC gates of the starting cell population, indicating where boundaries between "positive" and "negative" staining cell populations are defined.

Tick this box to confirm that a figure exemplifying the gating strategy is provided in the Supplementary Information.

## Magnetic resonance imaging

#### Experimental design

Design type Indicate task or resting state; event-related or block design.

Design specifications

Specify the number of blocks, trials or experimental units per session and/or subject, and specify the length of each trial or block (if trials are blocked) and interval between trials.

Behavioral performance measures | St

State number and/or type of variables recorded (e.g. correct button press, response time) and what statistics were used to establish that the subjects were performing the task as expected (e.g. mean, range, and/or standard deviation across subjects).

Acquisition				
Imaging type(s)	Specify: functional, structural, diffusion, perfusion.			
Field strength	Specify in Tesla			
Sequence & imaging parameters	Specify the pulse sequence type (gradient echo, spin echo, etc.), imaging type (EPI, spiral, etc.), field of view, matrix size, slice thickness, orientation and TE/TR/flip angle.			
Area of acquisition	State whether a whole brain scan was used OR define the area of acquisition, describing how the region was determined.			
Diffusion MRI Used	Not used			
Preprocessing				
Preprocessing software	Provide detail on software version and revision number and on specific parameters (model/functions, brain extraction, segmentation, smoothing kernel size, etc.).			
Normalization	data were normalized/standardized, describe the approach(es): specify linear or non-linear and define image types used for ansformation OR indicate that data were not normalized and explain rationale for lack of normalization.			
Normalization template	Describe the template used for normalization/transformation, specifying subject space or group standardized space (e.g. original Talairach, MNI305, ICBM152) OR indicate that the data were not normalized.			
Noise and artifact removal	Describe your procedure(s) for artifact and structured noise removal, specifying motion parameters, tissue signals and physiological signals (heart rate, respiration).			
Volume censoring	Define your software and/or method and criteria for volume censoring, and state the extent of such censoring.			
Statistical modeling & infere	ce			
Model type and settings	Specify type (mass univariate, multivariate, RSA, predictive, etc.) and describe essential details of the model at the first and second levels (e.g. fixed, random or mixed effects; drift or auto-correlation).			
Effect(s) tested	Define precise effect in terms of the task or stimulus conditions instead of psychological concepts and indicate whether ANOVA or factorial designs were used.			
Specify type of analysis: W	le brain ROI-based Both			
Statistic type for inference (See Eklund et al. 2016)	Specify voxel-wise or cluster-wise and report all relevant parameters for cluster-wise methods.			
Correction	Describe the type of correction and how it is obtained for multiple comparisons (e.g. FWE, FDR, permutation or Monte Carlo).			
Models & analysis				
n/a Involved in the study    Functional and/or effective connectivity   Graph analysis   Multivariate modeling or predictive analysis				
Functional and/or effective conn	Report the measures of dependence used and the model details (e.g. Pearson correlation, partial correlation, mutual information).			
Graph analysis  Report the dependent variable and connectivity measure, specifying weighted graph or binarized a subject- or group-level, and the global and/or node summaries used (e.g. clustering coefficient, effect.).				

Multivariate modeling and predictive analysis | Specify independent variables, features extraction and dimension reduction, model, training and evaluation

metrics.